The Accretion History of AGN: The Spectral Energy Distributions of X-Ray-luminous Active Galactic Nuclei

Connor Auge[1] , David Sanders[1] , Ezequiel Treister[2] , C. Megan Urry[3] , Allison Kirkpatrick[4] , Nico Cappelluti[5] ,
Tonima Tasnim Ananna[6] , Médéric Boquien[7] , Mislav Baloković[3] , Francesca Civano[8] , Brandon Coleman[4] ,
Aritra Ghosh[9,10] , Jeyhan Kartaltepe[11] , Michael Koss[12,13] , Stephanie LaMassa[14] , Stefano Marchesi[15,16,17] ,
Alessandro, Peca[5] , Meredith Powell[18] , Benny Trakhtenbrot[19] , and Tracey Jane Turner[12]

[1] Institute for Astronomy, University of Hawai`i, 2680 Woodlawn Drive, Honolulu, HI 96822, USA; cauge@hawaii.edu
[2] Instituto de Astrofísica, Facultad de Física, Pontificia Universidad Católica de Chile, Casilla 306, Santiago 22, Chile
[3] Physics Department and Yale Center for Astronomy & Astrophysics, PO Box 208120, New Haven, CT 06520-8120, USA
[4] Department of Physics & Astronomy, University of Kansas, Lawrence, KS 66045, USA
[5] Department of Physics, University of Miami, Coral Gables, FL 33124, USA
[6] Department of Physics and Astronomy, Dartmouth College, 6127 Wilder Laboratory, Hanover, NH 03755, USA
[7] Instituto de Alta Investigación, Universidad de Tarapacá, Casilla 7D, Arica, Chile
[8] NASA Goddard Space Flight Center, Greenbelt, MD 20771, USA
[9] Department of Astronomy, Yale University, New Haven, CT, USA
[10] Yale Center for Astronomy and Astrophysics, New Haven, CT, USA
[11] Laboratory for Multiwavelength Astrophysics, School of Physics and Astronomy, Rochester Institute of Technology, 84 Lomb Memorial Drive, Rochester, NY 14623, USA
[12] Eureka Scientific, 2452 Delmer Street, Suite 100, Oakland, CA 94602-3017, USA
[13] Space Science Institute, 4750 Walnut Street, Suite 205, Boulder, CO 80301, USA
[14] Space Telescope Science Institute, 3700 San Martin Drive, Baltimore, MD 21210, USA
[15] Dipartimento di Fisica e Astronomia (DIFA), Università di Bologna, via Gobetti 93/2, I-40129 Bologna, Italy
[16] Department of Physics and Astronomy, Clemson University, Kinard Lab of Physics, Clemson, SC 29634, USA
[17] INAF—Osservatorio di Astrofisica e Scienza dello Spazio di Bologna, Via Piero Gobetti, 93/3, I-40129 Bologna, Italy
[18] Kavli Institute for Particle Astrophysics and Cosmology, Stanford University, 452 Lomita Mall, Stanford, CA 94305, USA
[19] School of Physics and Astronomy, Tel Aviv University, Tel Aviv 69978, Israel
Received 2023 May 25; revised 2023 August 2; accepted 2023 August 14; published 2023 October 23

Abstract

Spectral energy distributions (SEDs) from X-ray to far-infrared (FIR) wavelengths are presented for a sample of 1246 X-ray-luminous active galactic nuclei (AGNs; $L_{0.5-10\,\mathrm{keV}} > 10^{43}$ erg s^{-1}), with $z_{\mathrm{spec}} < 1.2$, selected from Stripe 82X, COSMOS, and GOODS-N/S. The rest-frame SEDs show a wide spread ($\sim$2.5 dex) in the relative strengths of broad continuum features at X-ray, ultraviolet (UV), mid-infrared (MIR), and FIR wavelengths. A linear correlation (log–log slope of 0.7 ± 0.04) is found between L_{MIR} and L_X. There is significant scatter in the relation between the L_{UV} and L_X owing to heavy obscuration; however, the most luminous and unobscured AGNs show a linear correlation (log–log slope of 0.8 ± 0.06) in the relation above this scatter. The relation between L_{FIR} and L_X is predominantly flat, but with decreasing dispersion at $L_X > 10^{44}$ erg s^{-1}. The ratio between the "galaxy-subtracted" bolometric luminosity and the intrinsic L_X increases from a factor of $\sim$10 to 70 from log $L_{\mathrm{bol}}/$ (erg s^{-1}) = 44.5 to 46.5. Characteristic SED shapes have been determined by grouping AGNs based on relative strengths of the UV and MIR emission. The average $L_{1\mu\mathrm{m}}$ is constant for the majority of these SED shapes, while AGNs with the strongest UV and MIR emission have elevated $L_{1\mu\mathrm{m}}$, consistent with the AGN emission dominating their SEDs at optical and near-infrared wavelengths. A strong correlation is found between the SED shape and both the L_X and L_{bol}, such that $L_{\mathrm{bol}}/L_X = 20.4 \pm 1.8$, independent of the SED shape. This is consistent with an evolutionary scenario of increasing L_{bol} with decreasing obscuration as the AGN blows away circumnuclear gas.

Unified Astronomy Thesaurus concepts: Active galactic nuclei (16); AGN host galaxies (2017); X-ray active galactic nuclei (2035); Spectral energy distribution (2129); Surveys (1671)

Supporting material: machine-readable tables

1. Introduction

Nearly every galaxy has a supermassive black hole (SMBH) at its center with a mass ranging from 10^5 to 10^{10} $M_\odot$. These SMBHs undergo significant periods of growth as active galactic nuclei (AGNs) when large amounts of gas and dust accrete onto the SMBH. While many theoretical models require AGN feedback to play a significant role in galaxy evolution in order to match local observations, the exact impact of an AGN on the properties of the host galaxy is still uncertain (see reviews by Alexander et al. 2003; Kormendy & Ho 2013; Heckman & Best 2014). Some studies find suppressed star formation for the most luminous AGNs (e.g., Bongiorno et al. 2012; Page et al. 2012; Barger et al. 2015; Yang et al. 2017), and others report that AGN activity does not significantly affect the global star formation, or that it may even enhance star formation in some host galaxies (e.g., Lutz et al. 2010; Mullaney et al. 2012; Rovilos et al. 2012; Santini et al. 2012; Suh et al. 2019). To determine the extent of AGN feedback and the effect that this has on the host galaxy, it is vital to

disentangle the contributions of the AGN and host galaxy to the total emission. This is challenging, as many extragalactic sources contain a mix of star formation and obscured black hole growth. To fully understand the properties of both the AGN and the host galaxy, it is necessary to accurately identify the extent of the emission from the AGN, star formation, and stellar populations in the nearby environments. This can be done through a detailed analysis of their spectral energy distributions (SEDs), with a particular focus on the infrared properties (e.g., Assef et al. 2013, 2015; Hickox & Alexander 2018). If a complete understanding of the intrinsic properties of the AGNs and host galaxies is desired, it is also vital, in such an analysis, to ensure that each source is properly identified as being dominated by AGN activity, star formation in the host galaxy, or a strong combination of the two. If the AGN emission is not properly accounted for, then derived host galaxy properties, such as the star formation rate (SFR), can be overestimated by up to, if not greater than, ∼35% (Kirkpatrick et al. 2017; Cooke et al. 2020).

The accretion of gas and dust onto the SMBH produces a variety of emission properties that are directly tied to the physical characteristics of the AGN, including X-ray emission from the hot corona, ultraviolet (UV)−optical emission directly from the inner accretion disk, and mid-infrared (MIR) emission from a warm dusty torus (for review, see Netzer 2015). Far-infrared (FIR) emission from cold dust may also be directly associated with the AGN or with star formation in the host galaxy (e.g., Symeonidis et al. 2016; McKinney et al. 2021). The obscuration of AGNs may be driven by the SMBH accretion properties (Ricci et al. 2017) or by dust located in the torus, in polar regions, or at large distances from the galactic nucleus within the host galaxy (Goulding et al. 2012; Gilli et al. 2022). Furthermore, there have been studies suggesting that the nuclear dust is not uniformly distributed around the central engine, indicating the complex and clumpy structure of the dusty torus that may include polar dust extending above and below this torus (e.g., Ramos Almeida et al. 2009, 2011; Markowitz et al. 2014; Ichikawa et al. 2015; Asmus et al. 2016; Stalevski et al. 2017). Sanders et al. (1988) suggested an evolutionary scenario for AGNs in which the obscuration is an evolutionary phase triggered by an accretion event or a merger between two galaxies. Subsequently, the obscured AGN expels most of the obscuring material, evolving into a classic unobscured quasar (DiMatteo et al. 2005; Hopkins et al. 2006; Ananna et al. 2022a, 2022b).

Most known quasars at high redshift were found in optical surveys, primarily in the Sloan Digital Sky Survey (SDSS; Fan et al. 2003; Richards et al. 2004; Schneider et al. 2005), which was most sensitive to unobscured objects. However, significant periods of growth can also take place in obscured AGNs (Hopkins et al. 2008), and in fact it is now believed that the majority of SMBH growth is heavily dust obscured (e.g., Treister et al. 2004, 2009; Hickox & Markevitch 2007; Ananna et al. 2019). Therefore, many AGNs undergoing significant periods of growth are missed by classical optical surveys. Selecting AGNs by the hard X-ray emission minimizes this bias, as the X-rays that are produced in AGNs can pierce through the optically obscuring gas (typically with $N_{\mathrm{H}} \sim 10^{22}$), so long as it is not Compton-thick, with $N_{\mathrm{H}} > 10^{24}$ cm^{-2} (Bassani et al. 1999; Heckman et al. 2005). Powerful X-ray emission seems to be a common feature among nearly all AGNs and is produced by the inverse Compton scattering of

photons from the accretion disk in the surrounding corona (Nandra & Pounds 1994). Additionally, purely star-forming galaxies, which produce X-rays through a number of high-mass X-ray binaries, young supernova remnants, and hot plasma in star-forming regions, rarely reach comparable luminosities to those of powerful AGNs in the X-rays, with purely star-forming galaxies typically showing $L_{\mathrm{X}} < 10^{42}$ erg s^{-1} (e.g., Fabbiano et al. 1989; Ranalli et al. 2003). However, X-ray selection may still miss low-luminosity or heavily obscured AGNs that might instead be detected through their MIR colors (Lacy et al. 2004, 2013; Stern et al. 2005; Assef et al. 2010, 2013; Donley et al. 2012; Kirkpatrick et al. 2017; Yan et al. 2019; Carroll et al. 2021, 2023; Hviding et al. 2022).

To fully understand the energetics and demographics of AGNs, it is necessary to characterize their emission across the electromagnetic spectrum, particularly in the MIR and FIR, where much of the energy is emitted but not always observed. To this end, we present an analysis of the SEDs for a sample of ∼1200 hard-X-ray-selected AGNs from the Accretion History of AGN (AHA) wedding-cake survey (PI M. Urry). In Section 2 of this paper we describe the multiwavelength data from the four different observation fields used in this analysis. Section 3 presents the sample selection, along with the construction of the X-ray to FIR SEDs. An in-depth analysis of the SED properties with respect to redshift and bolometric luminosity is presented in Section 4. Section 5 presents a breakdown of the characteristic SED profiles and presents the emission properties in the context of the AGN life cycle. Finally, our results are summarized in Section 6. Throughout this analysis we assume a standard cosmology with $H_0 = 70$ km s^{-1} Mpc^{-1}, $\Omega_m = 0.3$, and $\Omega_\Lambda = 0.7$.

2. Data

This work utilizes detailed multiwavelength data from the AHA survey, which is composed of three survey fields of varying depths and sky coverage. Together, these fields create a "wedding-cake survey," where each field probes a different area and flux limit and therefore detects AGNs in a different luminosity and redshift range. The widest field is Stripe 82X (LaMassa et al. 2013b, 2013a, 2016; Ananna et al. 2017), a wide-area X-ray survey covering ∼31 deg^2 of the legacy SDSS Stripe 82 field (Jiang et al. 2014). The middle layer of the "wedding cake" is the COSMOS field (Scoville et al. 2007; Elvis et al. 2009; Civano et al. 2016), a deep, wide-field, multiwavelength survey covering a 2 deg^2 field centered on the J2000 coordinates R.A. = + 150.119 and decl. = + 2.205. The final layer is from the Great Observatories Origins Survey (GOODS; Giavalisco et al. 2004). The two GOODS fields, GOODS North and South (GOODS-N/S), utilize extremely deep observations from NASA's Great Observatories; together, these two fields cover a total of 320 arcmin^2 and contain the deepest flux limits in the AHA survey.

2.1. Stripe 82X

Stripe 82X contains three contiguous regions of XMM-Newton coverage, observed in XMM-Newton cycles 10 and 13 (AO10 and AO13) along with archival XMM-Newton and Chandra data. The details of the X-ray observations are described in LaMassa et al. (2013b, 2013a, 2016), with a final multiwavelength catalog and photometric redshifts presented by Ananna et al. (2017). Stripe 82X contains 6181 X-ray

sources. Of these, Peca et al. (2023) identified 2937 AGNs with reliable redshifts and sufficient counts to perform X-ray spectral modeling to determine the intrinsic X-ray luminosity that is corrected for galactic, host galaxy, and circumnuclear extinction along with estimates of the neutral hydrogen column density (N_H) for these sources.

In addition to the X-ray coverage, Stripe 82X also contains rich multiwavelength data with UV data from GALEX (Morrissey et al. 2007), optical data from deep coadded SDSS Stripe 82 catalogs (Jiang et al. 2014; Fliri & Trujillo 2016), near-infrared (NIR) data from UKIDS (Hewett et al. 2006; Casali et al. 2007; Lawrence et al. 2007) and the Vista Hemisphere Survey (VHS; McMahon et al. 2013), MIR data from Spitzer IRAC (Papovich et al. 2016; Timlin et al. 2016) and the Wide-field Infrared Survey Explorer (WISE; Wright et al. 2010), FIR coverage from Herschel Spire (Viero et al. 2014), and radio coverage at 1.4 GHz from Faint Images of the Radio Sky at Twenty cm (FIRST; Becker et al. 1995; Helfand et al. 2015).

Ananna et al. (2017) utilized these data to construct the latest version of the Stripe 82X multiwavelength catalog. The various multiwavelength associations were cross-matched using a statistical maximum likelihood estimator algorithm to report the most likely counterpart to each X-ray source (Sutherland & Saunders 1992), allowing for much more accurate cross-matches than a simple positional matching technique. The final catalog consists of far-UV (FUV) and near-UV (NUV) from GALEX (0.15 and 0.23 μm, respectively); u, g, r, i, and z from SDSS (0.34, 0.48, 0.62, 0.77, 1.1 μm, respectively); J, H, and K from VHS/UKIDSS (1.25, 1.63, 2.20 μm, respectively); CH1 and CH2 from IRAC (3.54 and 4.48 μm, respectively); and W1, W2, W3, and W4 from ALLWISE (3.35, 4.6, 11.6, and 22.1 μm, respectively). Finally, the matches to the FIR Herschel SPIRE data (250, 350, and 500 μm), which were not included in Ananna et al. (2017), are taken from LaMassa et al. (2016) based on the matching ID of each source. In this work we substitute the ALLWISE W3 and W4 data reported in Ananna et al. (2017) with those from Lang et al. (2016), who utilized a forced photometry technique, using measured SDSS source positions, star−galaxy classifications, and galaxy profiles to define the sources whose fluxes are to be measured in the WISE images. This results in a greater number of detections in the W3 and W4 bands and more sensitive flux limits.

2.2. COSMOS

The COSMOS Legacy survey is a 4.6 Ms Chandra program that imaged the COSMOS field. Details of this survey, including X-ray and optical/infrared photometric and spectroscopic properties, are described in Civano et al. (2016) and Marchesi et al. (2016a), and Lanzuisi et al. (2018) conducted an extended analysis of Chandra COSMOS Legacy sources with more than 30 net counts, utilizing improved background modeling and modeling techniques optimized for heavily obscured sources. These catalogs were built off the initial work done in the XMM-COSMOS survey (Cappelluti et al. 2007, 2009).

Weaver et al. (2022) presented the updated catalog of precise photometric redshifts and 30-band photometry for more than half a million secure objects within the 2 deg^2 COSMOS field. This updated catalog presents significantly deeper optical and NIR images along with a reprocessing of all Spitzer data. The aperture extraction techniques described in Weaver et al. (2022) ensure that accurate data are presented for each photometric filter, with a low probability of contamination from differing sources, particularly in the UV to MIR wavelengths. Marchesi et al. (2016a) provide the cross-matches between the COSMOS Legacy survey and the original COSMOS mulitwavelength catalog from Laigle et al. (2016). The IDs from this cross-match were used to identify the mulitwavelength counterparts in the Weaver et al. (2022) catalog, the X-ray sources from Marchesi et al. (2016a, 2016b) and Lanzuisi et al. (2018), and the FIR data that were presented in Laigle et al. (2016) but were absent from the updated catalog. The final catalog includes the GALEX FUV and NUV bands, CFHT U band, five Subaru Hyper Suprime-Cam (HSC) bands (g, r, i, z, y), four UltraVista bands (Y, H, J, K_s), four Spitzer IRAC bands (3.6, 4.5, 5.8, and 8.0 μm), the 24 μm Spitzer MIPS observations, and the Herschel PACS (100 and 160 μm) and SPIRE (250, 350, and 500 μm) observations. The details of these mulitwavelength observations can be found in Weaver et al. (2022) and references therein. Additional spectroscopic redshifts were also gathered from Hasinger et al. (2018) and match to IDs from the COSMOS catalogs.

Significant efforts have previously been made to analyze the SEDs of X-ray-luminous AGNs in the COSMOS field, with a particular focus on unobscured AGNs and determining their characteristic multiwavelength features (e.g., Elvis et al. 2012; Hao et al. 2013, 2014) or comparing the properties and population statistics of obscured and unobscured AGNs (e.g., Lusso et al. 2013; Suh et al. 2019). This analysis builds off of these previous works by placing the COSMOS field in the greater context of the entire AHA wedding-cake survey.

2.3. GOODS

The GOODS-N and GOODS-S fields are centered around the Chandra Deep Field (CDF) surveys (see, e.g., Brandt & Alexander 2015; Xue 2017, for reviews). These two fields consist of the 7 Ms Chandra Deep Field South (CDF-S; Luo et al. 2017), which is the deepest X-ray survey to date, and the 2 Ms Chandra Deep Field North (CDF-N; Xue et al. 2016). These deep X-ray surveys allow for a detailed analysis of the X-ray spectra. With these observations, accurate estimates of N_H and intrinsic X-ray luminosity can be made. Li et al. (2020) improved this analysis for the most heavily obscured AGNs within CDF-N/S. Estimates of the intrinsic X-ray luminosity and column density are taken from Li et al. (2020) when available.

GOODS-N/S compose two of the five Cosmic Assembly Near-infrared Deep Extragalactic Legacy Survey (CANDELS; Grogin et al. 2011; Koekemoer et al. 2011) fields. CANDELS is a Hubble Space Telescope (HST) 902-orbit legacy program designed to study galaxy formation and evolution over a wide range of redshifts using the NIR HST/WFC3 camera to obtain deep imaging of faint and distant objects. Guo et al. (2013) presented a catalog of the UV to MIR data for the CANDELS/GOODS-S field by combining the HST data (ACS: F435W, F606W, F775W, F814W, F850LP, and WFC3 F098M) with archival data from CTIO/MOSAIC, VLT/VIMOS, VLT/ISAAC K_s, VLT/HAWK-I K_s, and Spitzer/IRAC 3.6, 4.5, 5.8, and 8.0 μm. The Spitzer/MIPS 24 and 70 μm and Herschel 100, 160, 250, 350, and 500 μm data come from matches to Elbaz et al. (2011).

Barro et al. (2019) presented a catalog of the CANDELS/ GOODS-N field containing the photometry from the UV to FIR. This includes data from the U band from KPNO and LBC; HST/ACS F435W, F606W, F775W, F814W and F850LP; HST/WFC3 F105W, F125W, F140W, and F160W; Subaru/ MOIRCS K_s; CFHT/MegaCam K; Spitzer/IRAC 3.6, 4.5, 5.8, and 8.0 μm; FIR Spitzer/MIPS 24 μm; Herschel/PACS 100 and 160 μm; and SPIRE 250, 350, and 500 μm.

These two catalogs were combined with additional data in the optical to MIR gathered from Damen et al. (2011), Hsu et al. (2014), Skelton et al. (2014), Yang et al. (2014), and Straatman et al. (2016), along with data in the FIR from Oliver et al. (2012) and the "Super-deblended" FIR data presented in Liu et al. (2018). This extensive list of multiwavelength sources for the GOODS fields was matched using a nearest neighbor approach, utilizing a matching radius of 2″ for the UV−NIR data and a matching radius of 5″ for the MIR−FIR data. These matches were then confirmed by comparing the redshifts reported in each respective catalog when available.

For all three surveys, significant work has been previously done to ensure a low probability of sources being incorrectly matched across different photometric filters, through the use of maximum likelihood matching techniques (Ananna et al. 2017), carefully defined aperture extraction (Weaver et al. 2022), or positional matching with narrow matching radii plus comparison of spectroscopic information, such as redshift. The Herschel SPIRE FIR images are the most likely source of mismatches, due to the lower spatial resolution of the Herschel SPIRE instrument relative to other wavelengths. To check for contamination in SPIRE-detected sources, we have compared the source density of the higher-resolution MIR detections from the Spitzer MIPS 24 μm data to the beam size of the Herschel instrument. We find that, on average, only one source with a large enough flux to strongly contribute to the reported FIR flux of the sources in the sample is found within the typical beam size of the Herschel SPIRE data. This is consistent with deblending work in the COSMOS field reported by Jin et al. (2018). Therefore, while contamination may play a role in some sources, it does not affect the majority of the sample (<10%).

3. Methods

3.1. Sample Selection

As the goal of this work is to comprehensively analyze the SEDs of luminous AGNs from the AHA fields, we limit our sample to those sources with photometric coverage in the regions of the electromagnetic spectrum necessary for such an analysis, namely the UV and MIR regions, where the emission from the accretion disk and dusty torus, respectively, is most prominent. Each of the survey fields has extensive coverage in the UV and optical; therefore, having adequate data to analyze the accretion disk emission will not be an issue for a majority of sources. However, the MIR coverage for these sources is much sparser, with large gaps between the observed filters. As discussed in Section 2, COSMOS and GOODS-N/S both have MIR data in the Spitzer IRAC channels going out to 8 μm and Spitzer MIPS data at 24 μm. There is then a large gap in data until the FIR coverage with Herschel. Stripe 82X has similar coverage with the WISE W3 and W4 bands at 11 and 22 μm. This poses a larger challenge for analyzing the MIR data of AGNs at high redshift. At $z > 1.2$, the Spitzer MIPS 24 μm data
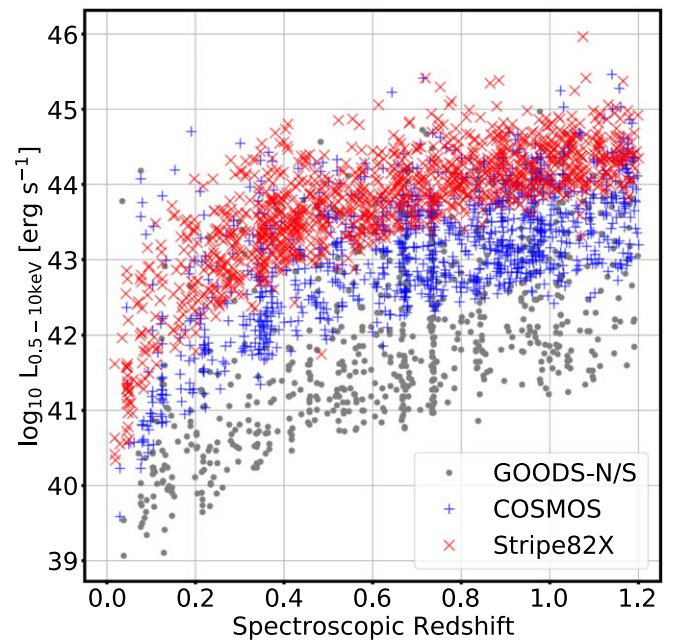

Figure 1. The intrinsic 0.5–10 keV X-ray luminosity as a function of spectroscopic redshift for the sources in the AHA survey. The red crosses are the sources from the largest and shallowest layers of the wedding cake, the Stripe 82X survey; the blue plus signs are from the middle layer, COSMOS; and the gray circles are from the GOODS-N/S fields. Only sources with confirmed multiwavelength counterparts that have been observed with Herschel are shown.

and the WISE W4 data are shifted to rest-frame wavelengths blueward of 10.9 and 10 μm, respectively. For this reason, we limit our sample to sources in the AHA fields with a secure spectroscopic redshift measurement less than 1.2, ensuring that we have a photometric observation in the rest-frame MIR near 10 μm for all sources in our sample. This will allow us to better characterize the MIR SED profiles and investigate how the 10 μm traces AGN properties.

In order to analyze the cold dust emission, we further limit the sample by removing sources that were not within the fields covered in the FIR with the Herschel SPIRE instrument (250, 350, and 500 μm). The entire COSMOS field and both GOODS fields were covered with SPIRE; however, only a portion of Stripe 82X was observed in these bands. The X-ray fields within Stripe 82 that fall in an R.A. range of $13°-37°$ and a decl. of $-2°$ to $2°$ are included in this analysis. This is the full XMM-AO13 area, as the fields for these observations were specifically chosen to overlap with the Herschel and Spitzer coverage within Stripe 82. Sources that do not fall in these regions are removed from the sample, so upper limits can be used to accurately constrain the FIR emission.

Figure 1 shows the intrinsic X-ray luminosity as a function of spectroscopic redshift for all sources with $z < 1.2$ and observations (though not necessarily detections) with Herschel SPIRE. This figure also illustrates the benefits of a wedding-cake-style X-ray survey by clearly showing the effects of the different flux limits and the areas of the different fields, with Stripe 82X capturing the most luminous sources, thanks to the increased volume accessed by the wide survey field. GOODS-N/S captures the least luminous sources, thanks to the increased depth. The COSMOS field then bridges the gap between the two. It can be seen that the combined surveys are

Table 1
The Number of Sources from Each AHA Field Included in the Analysis

Field	$z < 1.2$	$L_X > 10^{43}$ (erg s^{-1})	Rest Frame 6 μm
(1)	(2)	(3)	(4)
Stripe 82X	1169	998	529
COSMOS	1128	664	624
GOODS−N/S	704	152	93
Total	3001	1814	1246

Note. Column (1): the AHA field. Column (2): number of sources from each field with a spectroscopic redshift of $z \leqslant 1.2$ and located in a field observed by Herschel SPIRE. Column (3): the number of sources from Column (2) that satisfy the minimum intrinsic 0.5–10 kev X-ray luminosity condition of $L_X > 10^{43}$ erg s^{-1} for the sample selection. Column (4): the number of these sources that have secure mulitwavelength counterparts and detections near rest frame ∼6 μm.

substantially complete at X-ray luminosities greater than 10^{42} erg s^{-1} up to $z \sim 1.2$.

AGNs are identified from this $z < 1.2$ subsample based on their intrinsic 0.5–10 keV X-ray luminosity taken from Marchesi et al. (2016a), Ananna et al. (2017), Luo et al. (2017), Xue (2017), Lanzuisi et al. (2018), Peca et al. (2023), and Li et al. (2020). AGNs can generate X-ray luminosities up to 10^{46} erg s^{-1}, while star-forming galaxies rarely produce X-ray luminosities greater than 10^{42} erg s^{-1} (Ranalli et al. 2003; Persic et al. 2004). For this sample, all sources with intrinsic X-ray luminosities in the 0.5–10 keV band with $L_X < 10^{43}$ erg s^{-1} are removed from the sample to prevent contamination by even the most luminous purely star-forming galaxies. While this limit likely removes some low-luminosity AGNs, it will ensure a clean sample of purely luminous AGNs and little to no contamination from non-AGN sources. This is also where the sample is most complete, allowing us to include AGNs that are luminous in the X-rays, even though the non-AGN emission may dominate at other wavelengths (Brandt & Alexander 2015).

Finally, sources are removed from the sample if they do not have a photometric detection within ±2 μm of 6 μm in the rest frame. 6 μm is a key AGN diagnostic wavelength that has been shown to correlate strongly with X-ray properties. In order to conduct a thorough analysis of AGN properties in the MIR while being able to compare to previous work, we include this additional requirement for the sample.

Table 1 shows the contribution to the total sample of sources from each of the AHA fields. About half of the total sample comes from the COSMOS field, which has the most complete photometric and spectroscopic data set at the X-ray luminosities we are analyzing. Many GOODS sources fall below the X-ray luminosity limit, as can be seen in Figure 1. Additionally, many of the sources from Stripe 82X were excluded owing to a lack of detections with low error in the MIR WISE data near a rest frame of 6 μm. This requirement of MIR data may preferentially remove most dust-poor systems from the sample; however, sources with similar emission properties to those removed from Stripe 82X are found in the COSMOS and GOODS-N/S fields owing to the greater sensitivity of Spitzer in these fields. We additionally find similar distributions in the intrinsic X-ray luminosity for the sources within the final sample to those that are removed;
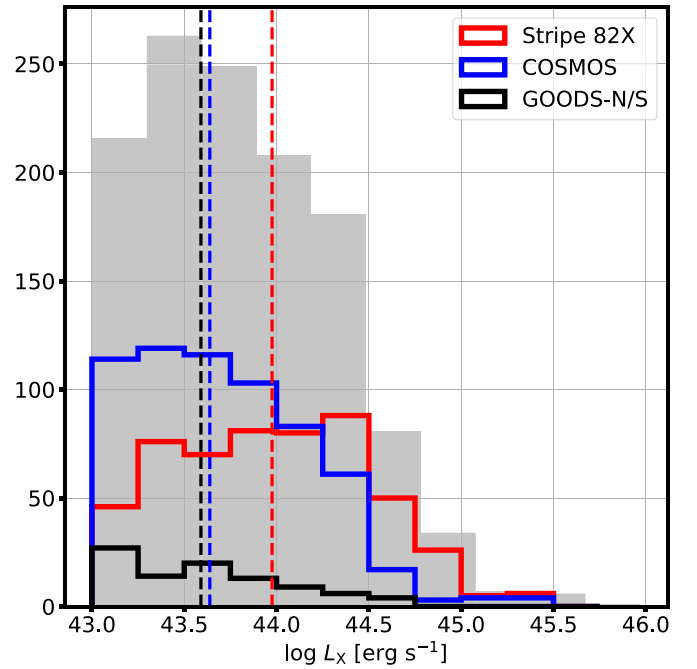

Figure 2. Histogram of the intrinsic 0.5–10 keV X-ray luminosity for the 1246 sources in our final sample. The gray histogram is the total sample; the histograms of the sources from each AHA field (Stripe 82X—red; COSMOS—blue; GOODS-N/s—black) are also shown. The median of each distribution from the respective AHA fields is shown as a vertical dashed line in the same corresponding color.

therefore, they are likely sampling the same population of AGNs.

Figure 2 shows the distribution of intrinsic X-ray luminosity for the final sample of 1246 AGNs. Similar to the distribution of the total AHA sample seen in Figure 1, the AGNs from Stripe 82X have a larger median X-ray luminosity, with the AGNs from GOODS-N/S showing the lowest median X-ray luminosity.

3.2. Constructing the SEDs

The SEDs are constructed by combining the X-ray to FIR data for all sources with each photometric data point corrected to the rest frame using the known spectroscopic redshift. Each flux measurement is also converted to a luminosity in erg s^{-1} using the same spectroscopic redshift and then normalized by the 1 μm luminosity. As the 1 μm emission is likely dominated by stellar light from the host galaxy, with little contamination from all but the most luminous AGNs (Neugebauer et al. 1989), normalizing the SED at this wavelength allows for the expected features of the AGN emission in the UV and MIR to be easily identified (i.e., the emission from the accretion disk and dusty torus). Contributions of AGN emission at 1 μm and how this affects the normalization of the sample are discussed in Section 5.1.

In order to simplify the process of normalizing all sources over a broad redshift range at the same rest-frame luminosity, the SED is generated for every source through a simple logarithmic interpolation between each secure photometric data point available for that source. The 1 μm luminosity is then taken from this interpolated SED. This same process is followed for the luminosities at other specified wavelengths that are analyzed throughout this work. While individual sources may not have a detection in a filter that falls at the
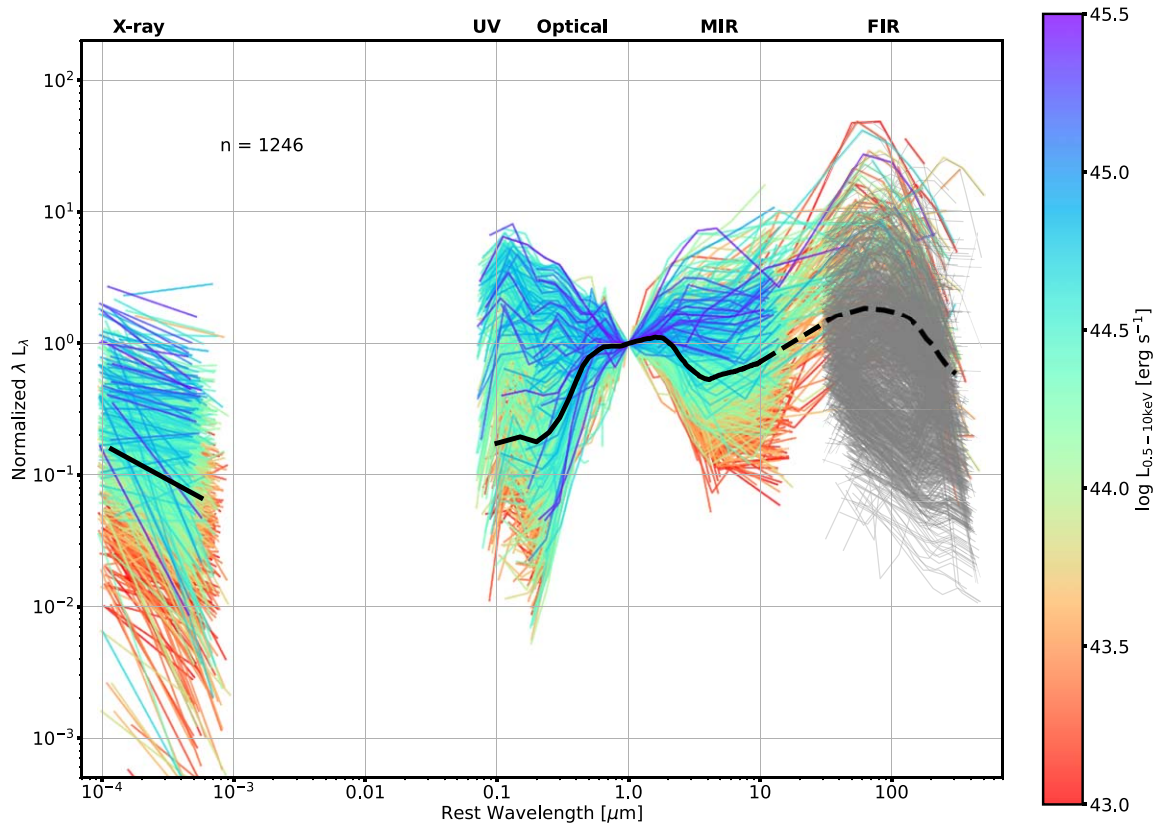
Figure 3. The SEDs normalized at 1 μm for the sources within our sample that match the criteria outlined in Section 3.1 and Table 1. The color of each SED is the intrinsic 0.5–10 keV X-ray luminosity. The solid black line is interpolation of the median SED in the X-ray and in the UV−MIR region. The dashed black line is the interpolation of the median SED of the detections and the 1σ upper limits in the FIR normalized at 1 μm. The normalized FIR upper limits for individual sources are shown in gray. A wide range of emission properties in the X-ray, UV, MIR, and FIR can be seen around the total median SED.

specified wavelength when brought to the rest frame, each source has secure photometric detections (or upper limits) at observational filters that fall shortward and longward of each specified wavelength, allowing for an estimation of the luminosity at the specified wavelength to be made. If there are no data, or large gaps in the data, shortward or longward of a specified luminosity, then a linear extrapolation is used.

All 1246 AGNs are shown in Figure 3 colored by the intrinsic 0.5–10 keV X-ray luminosity, with the median SED shown in black. Figure 4 shows the distribution of the 1 μm luminosities used for the normalization. The standard deviation of the distribution is under an order of magnitude. As stellar emission peaks near 1 μm, this luminosity can be used as a proxy for the stellar mass of these sources, assuming that no AGN emission is strongly contaminating the emission at this wavelength. While this may be a safe assumption for lower-luminosity AGNs, Sanders et al. (1989) show that the outer regions of the accretion disk (0.1–1 pc) can emit strongly between 0.5 and 5 μm through thermal emission. This potential contribution from the AGN near 1 μm is examined more closely in Section 5.1.

While there are adequate detections from X-ray to MIR to accurately interpolate the SED for each source, $\sim$70% of the sample is not detected in any of the three Herschel SPIRE bands. However, by design, each source in the sample was observed in the FIR with Herschel. This allows us to utilize image stacking to place better constraints on the flux from the FIR. We bin sources by redshift and MIR luminosity and stack the 250 μm images for each bin at the locations of the optical
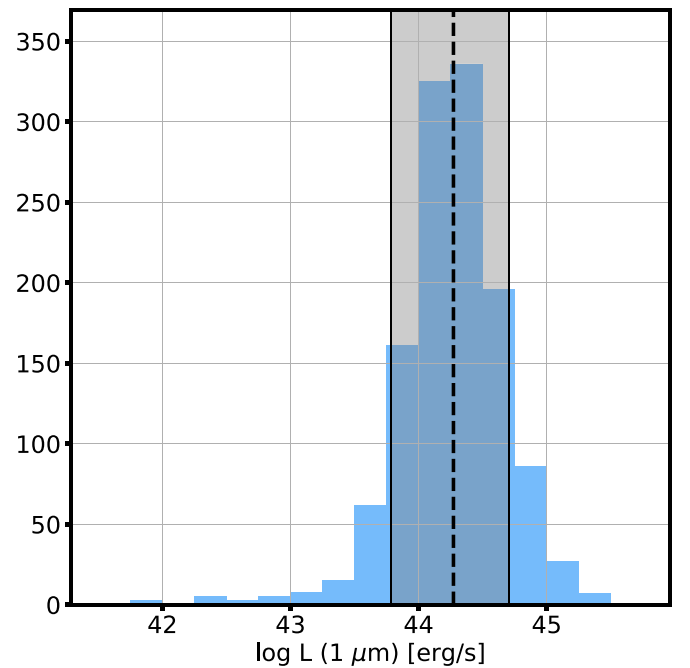

Figure 4. A distribution of the 1 μm luminosities for the 1246 AGNs in our sample. The mean of the distribution is shown as a vertical dashed line, and the shaded region shows the 1σ spread about the average. The 1σ distribution spans $\pm$ 0.46 dex around the mean of log $L(1\mu m)/(\mathrm{erg\ s^{-1}}) = 44.2$.

coordinates for each source. This stacking procedure is described in more detail in Appendix B. While the image stacking was utilized for the Stripe 82X sources to place
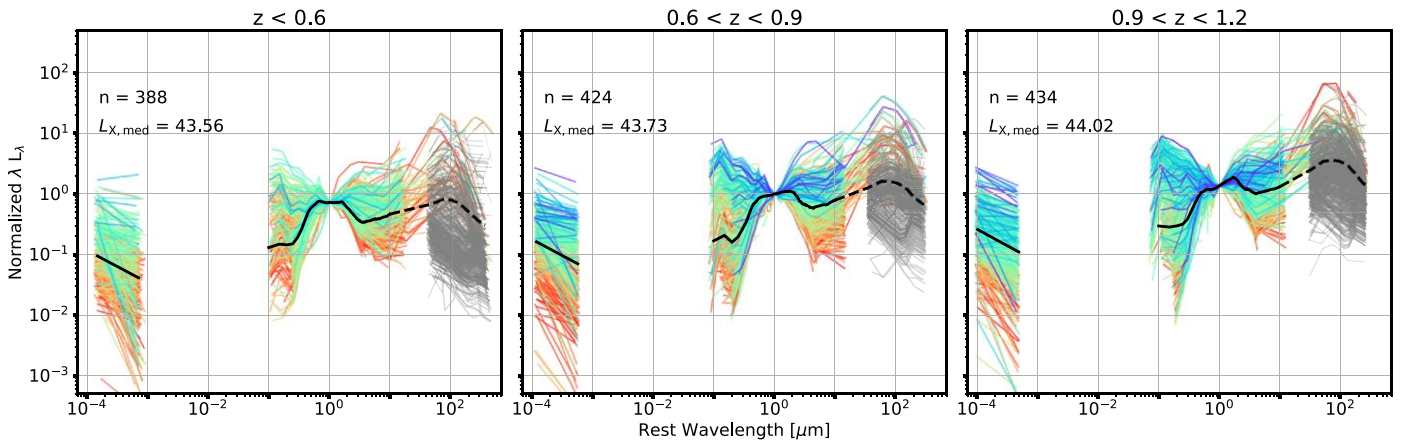
Figure 5. SEDs separated into three redshift bins. Each SED is normalized at 1 μm, with the normalization of each bin scaled to the normalization of the central bin. The color of each SED is the intrinsic 0.5–10 keV X-ray luminosity with the same color bar found in Figure 3. The solid black line is the median SED for the sources in each bin. The dashed black line is the median of the detections, stacked fluxes, and 1σ upper limits in the FIR. The FIR upper limits for individual sources are shown in gray. No major change in the median SED can be seen between the three redshift bins.
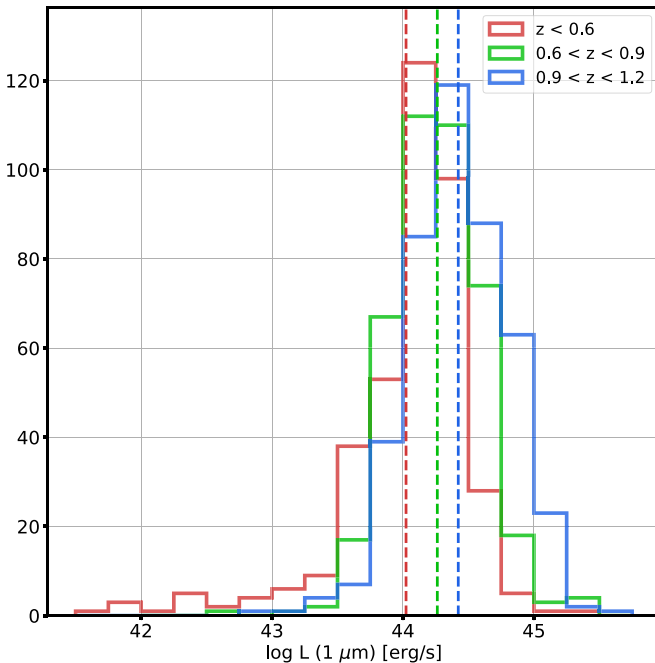
Figure 6. Distribution of the 1 μm luminosities for the 1246 AGNs in our sample separated into three redshift bins. The mean of each distribution is shown as a vertical dashed line with the same corresponding color as the histogram (log $L_{1\ \mu m}/(\mathrm{erg\ s^{-1}}) = 44.02$, 44.27, and 44.42 for each redshift bin in increasing order).

improved constraints on FIR emission, this process was unable to be performed on the sources from COSMOS or GOODS-N/S, as no statistically significant signal above the background noise could be found even in the stacked images. Therefore, we utilize the 1σ upper limits in the Herschel SPIRE bands for the sources from COSMOS and GOODS-N/S and the flux measurements from the stacked sources in Stripe 82X for the sources undetected in the FIR throughout the rest of the analysis. The 1σ upper limits were chosen as a conservative limit so as not to overestimate the FIR luminosity for these sources, whose emission could not be detected, even when stacked. These upper limits were also compared to the nearby galaxy NGC 518. We found the ratio of the rest-frame 100 μm emission to the 1 μm emission comparable to that found using

the upper limits in our sample, showing that the FIR luminosity is not drastically underestimated when utilizing 1σ upper limits. The dashed black line in Figure 3 is the median of the detections and the 1σ upper limits for each source renormalized by the 1 μm luminosity.

4. Analysis

4.1. SED Evolution with Redshift

In order to account for any potential change in the SED shape due to evolution with redshift, the sample of 1246 AGNs is separated into three redshift bins: $0.0 < z < 0.6$ (388 sources), $0.6 < z < 0.9$ (424 sources), and $0.9 < z < 1.2$ (434 sources). These three bins were defined so that each contains a roughly equal number of sources and is large enough for a statistical analysis of the multiwavelength properties while still allowing for insight into the evolution of these sources across cosmic time. The normalized SEDs for these three redshift bins can be seen in Figure 5. The median SED is largely the same for all three redshift bins, though a slight increase in the relative amount of NIR emission at ~ 2 μm of ~ 0.1 dex can be seen from the lowest to highest redshift bin. Additionally, the average FIR luminosity increases with redshift by ~ 0.35 dex. This is to be expected, as the dust content of star-forming galaxies increases with redshift, which will contribute to the total FIR luminosity of the source. The $0.9 < z < 1.2$ bin has both the largest total number of sources and the largest range of X-ray luminosities, compared to the lower two bins.

Figure 6 shows the distributions of 1 μm luminosities for the AGNs in each redshift bin. As expected, a slight trend of increasing luminosity with redshift is apparent, with the mean 1 μm luminosity increasing by ~ 0.3 dex from the lowest to highest redshift bin and the low-luminosity tail of the distribution falling in the lowest redshift bin. While there is an increase in the 1 μm luminosity with redshift, this increase is relatively small and within the dispersion of the individual distributions (mean log $L_{1\ \mu m}/(\mathrm{erg\ s^{-1}}) = 44.02 \pm 0.56$, 44.27 ± 0.35, and 44.42 ± 0.37 for each bin with increasing redshift). Due to the consistent luminosity of the host galaxies and that the wide range of SED profiles observed in Figure 3 is present in all three redshift bins, we conclude that the wide range of emission properties observed in the sample is not
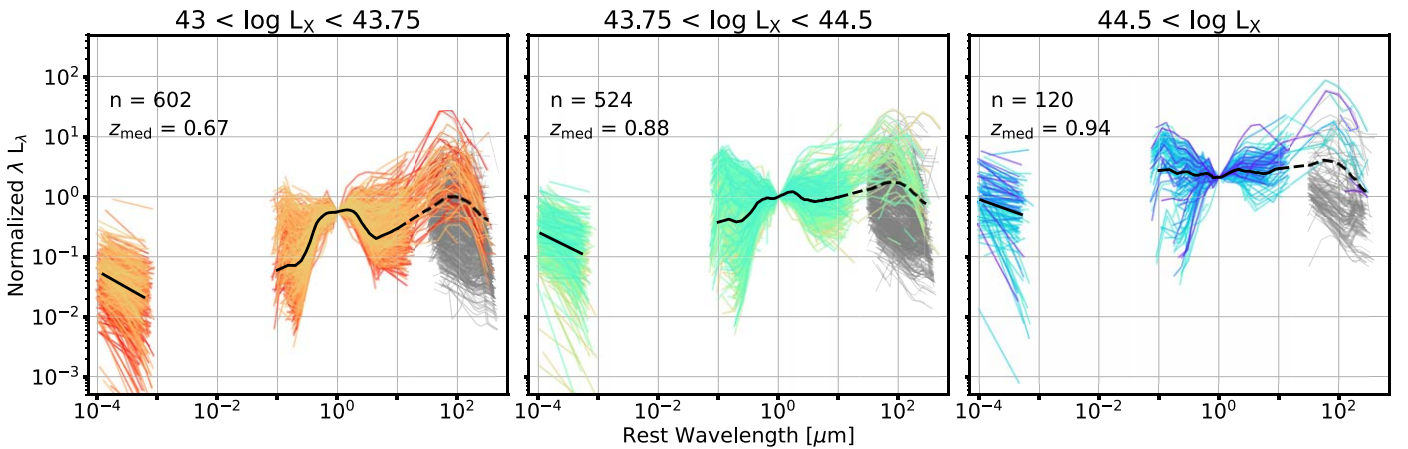
Figure 7. SEDs separated into three bins of increasing intrinsic 0.5–10 keV X-ray luminosity. Each SED is normalized at 1 μm, with the normalization of other bins scaled to the normalization of the central bin. The color of each SED is the intrinsic 0.5–10 keV X-ray luminosity with the same color bar found in Figure 3. The solid black line is the median SED for the sources in each bin. The dashed black line is the median of the detections and the 1σ upper limits. The FIR upper limits for individual sources are shown in gray. An evolution in the median SED can be seen with L_X; however, a large spread in the range of each emission property is still visible in each bin.

driven by redshift evolution. Therefore, we do not divide the AGNs into these redshift bins through the rest of the analysis and instead further analyze the emission properties of all AGNs uniformly.

4.2. SED Evolution with X-Ray Luminosity

To analyze the change of the SED profile with the intrinsic power of the AGN, the sample is separated into three bins of intrinsic 0.5–10 keV X-ray luminosity. Figure 7 shows the SEDs separated into these three bins, defined as $43 < \log L_X < 43.75$ (602 sources), $43.75 < \log L_X < 44.5$ (524 sources), and $44.5 < \log L_X$ (120 sources), where the X-ray luminosity is in units of erg s^{-1}. A clear evolution is visible in the median SED across the L_X bins, with the lowest bin showing the weakest UV and MIR emission relative to the 1 μm luminosity. The emission in these two regions increases as the intrinsic X-ray luminosity grows, with the largest L_X bin showing an approximately flat median SED in log–log space. As was done in Figure 5, the normalization in each bin shown in Figure 7 is scaled by the 1 μm normalization in the central bin, showing that the luminosity at all wavelengths also increases with increasing L_X.

While there are clear differences in the median SED, the total range of SED shapes is much more consistent across each L_X bin, with each bin showing a dispersion of more than 2 orders of magnitude in both the relative UV and MIR luminosity. This wide range in the slope of the UV and MIR continua shows that all three bins contain both obscured and unobscured AGNs. The most significant difference between the bins is in the number of FIR detections and the fact that the lowest L_X bin contains few sources with a strong peak in the UV (i.e., 0.1 μm) that can be seen in the other two bins. This shows some correlation in the observed UV luminosity or distribution of obscuring dust, with the intrinsic X-ray luminosity. This is examined in further detail in Section 4.3. Even with these few differences, it is clear that each bin in X-ray luminosity captures an extensive range of different AGN emission features.

4.3. AGN Emission

The main wavelength regions of interest when analyzing AGN properties are the UV emission originating through the thermal properties of the accretion disk, the MIR emission from the warm dusty torus, and the FIR emission, which may be associated with a more distant, cold dust component around the SMBH or with star formation in the host galaxy. We directly compare each of these emission components to the intrinsic 0.5–10 keV X-ray luminosity to determine how the reprocessed emission correlates with the intrinsic power of the AGN.

Figure 8 shows the observed UV (0.25 μm), MIR (6 μm), and FIR (100 μm) luminosity with respect to the intrinsic X-ray luminosity of each AGN. The most luminous AGNs that trace the upper bound of the relation seen in the top panel of Figure 8 show a log–log slope of 0.8 ± 0.06 and closely match with the relation presented in Just et al. (2007), which was derived using luminous, unobscured quasars from SDSS. However, there is significant scatter below this relation, even out to high L_X, with AGNs falling more than an order of magnitude below this upper bound. This high dispersion in the relation is likely due to obscuration around the central engine. While the X-ray luminosity shown in Figure 8 is the intrinsic luminosity that has been corrected for absorption, the UV is the observed luminosity. Therefore, for a given intrinsic L_X, we would expect a wide range of observed UV properties, as these AGNs are likely to show a wide range in the level of dust obscuration (further discussed in Sections 4.4 and 5.4). This relation between the X-ray emission and the UV–optical emission in unobscured AGNs has also been analyzed in Steffen et al. (2006) and Lusso & Risaliti (2017), both of which show a slope similar to the high-luminosity sources in this sample.

The middle panel of Figure 8 shows the relation between the intrinsic X-ray luminosity and the MIR luminosity, which is much less affected by extinction and obscuration than the UV luminosity. Correlations between MIR emission and AGN X-ray luminosity have been previously analyzed in many different studies (e.g., Lutz et al. 2004; Fiore et al. 2009; Gandhi et al. 2009; Lanzuisi et al. 2009; Lusso et al. 2011; Asmus et al. 2015; Stern 2015). The MIR properties of our sample show a log–log slope of 0.7 ± 0.04 and agree with the
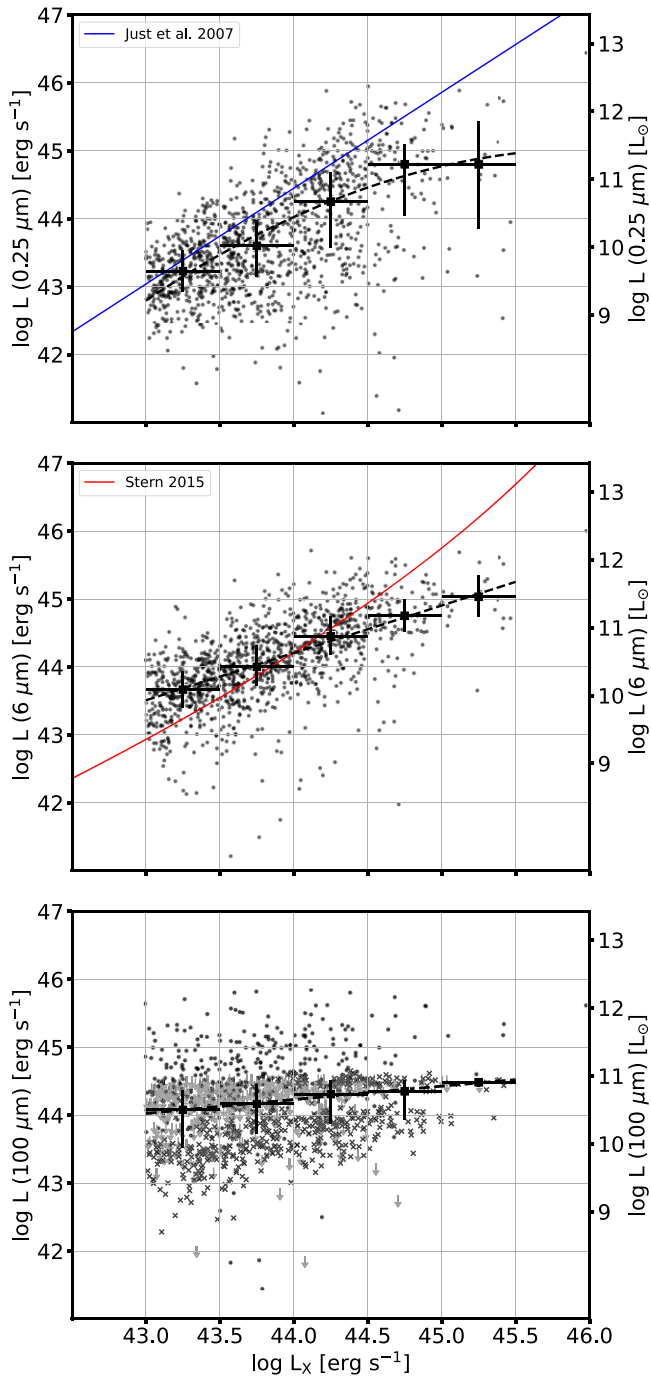
Figure 8. The 0.25 μm (top), 6 μm (middle), and 100 μm (bottom) as a function of the intrinsic 0.5–10 keV X-ray luminosity for all 1246 AGNs in the sample. The black squares show the median X-ray luminosity in bins of 0.5 dex along the x-axis. The vertical error bars show the 25th–75th percentile spread in each bin, and the horizontal error bars show the width of the bin. The black dashed line is a fit to these median points. The blue line shows the relation between the X-ray and UV luminosity from Just et al. (2007), derived from unobscured AGNs. The red line shows the relation between the X-ray luminosity and the 6 μm luminosity derived from Stern (2015). The upper limits in the FIR are shown by downward-pointing arrows, and the crosses show the sources from Stripe 82X that utilize image stacking. The emission at shorter wavelengths (UV–MIR) is AGN dominated in this sample, though the UV is heavily affected by dust. The weaker correlation at 100 μm likely means that this emission is not entirely dominated by the AGN across the full luminosity range.

relation derived by Stern (2015), only deviating slightly for the most X-ray-luminous sources. This relation is consistent with the MIR–X-ray luminosity correlation showing less scatter than

the UV-to-X-ray correlation, as the MIR emission is significantly less affected by obscuration than the UV emission.

The relation between the FIR luminosity and the intrinsic X-ray luminosity shown in Figure 8 is more challenging to analyze owing to the large number of FIR upper limits of varying depth in each respective field that are present in our sample. A general flat relation in log–log space is seen with a large dispersion of more than two orders of magnitude in each direction around the median. However, this dispersion decreases at high L_X. There are fewer AGNs with low FIR luminosity ($L_{FIR} < 10^{43.5}$ erg s^{-1}) at $L_X > 10^{44}$ erg s^{-1}, showing a lower bound that raises with increasing X-ray luminosity. This slight trend may imply a connection between the intrinsic X-ray luminosity and cold dust emission, with large X-ray luminosities correlating with a lack of low FIR luminosities. However, this exact relation depends on many additional factors, such as the dust mass and covering factor of the cold dust. Further discussion concerning how the cold dust component depends on the AGN activity is discussed further in Section 5.3.

4.4. Obscuring Column Density

The column density of neutral hydrogen N_H is often used as a tracer for the level of obscuration of an AGN and is found through detailed spectral fitting in the X-rays or approximated from the hardness ratio (i.e., the ratio of counts or count rate in the hard and soft X-ray bands). Most detailed analyses of AGN X-ray properties report an estimate of N_H for sources with high-quality X-ray spectra. However, determining this value accurately is strongly dependent on the quality of the X-ray data, as a large number of X-ray photons are needed to properly determine the spectral shape. This leads to many sources having only upper limits or no reported estimate of N_H, particularly the fainter sources in the sample. In total, about 57% of our sample has a secure measurement of the obscuring column density, while an additional ~32% of the sample has a reported upper or lower limit for N_H. The distribution of these limits is consistent with the distribution of the confirmed measurements, but lacking a peak at $N_H = 10^{20}$ cm^{-2}, seen in Figure 9. As unobscured AGNs are typically assigned to these low column density bins, this peak is likely not physical, but rather represents the number of unobscured AGNs in the sample. Each respective X-ray catalog has details about how these measurements and upper limits were made (Stripe 82X, Peca et al. 2023; COSMOS, Marchesi et al. 2016a, 2016b; Lanzuisi et al. 2018; GOODS-N, Xue et al. 2016; Li et al. 2020; GOODS-S, Luo et al. 2017; Li et al. 2020).

Figure 9 shows the distribution of the obscuring column density for each of the AGNs in our sample with a reliable estimate, or an upper limit. A bimodal distribution is visible, with a peak at $N_H = 10^{20}$ cm^{-2}. This is often the lowest value found and thus corresponds to an unobscured AGN. The second peak falls just above $N_H = 10^{22}$ cm^{-2}. This value corresponds to an obscured Compton-thin AGN with moderate amounts of obscuration. The tail of the distribution extends to just above $N_H = 10^{24}$ cm^{-2}, which is a heavily obscured, Compton-thick AGN. The declining distribution at high N_H is likely due to the bias against detecting heavily obscured AGNs in X-ray flux-limited surveys, rather than a decline in the actual numbers of heavily obscured AGNs (Hickox & Alexander 2018). Very few Compton-thick sources are detected in the AHA sample, as at this redshift range telescopes that probe
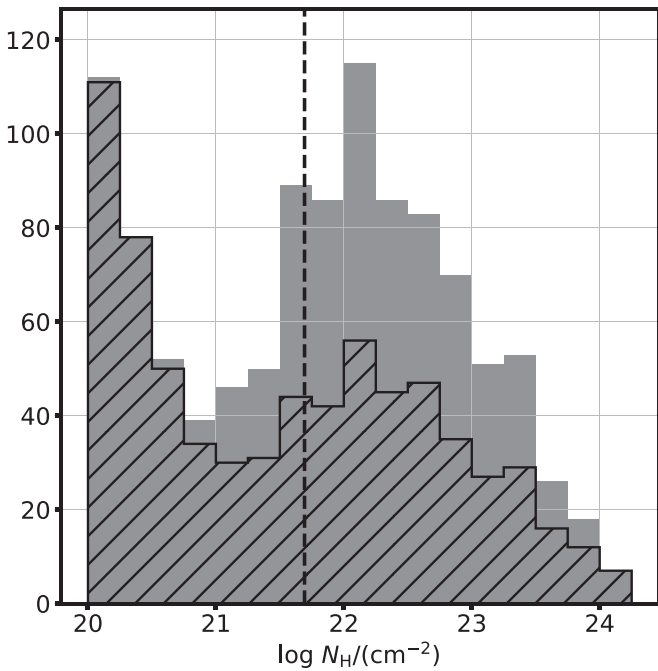
Figure 9. The distribution of obscuring column density, $N_{\rm H}$, for the measured estimates (∼56% of the sample) and the upper limits (∼32% of the sample). The total sample is shown in gray, while the measured estimates are shown as the hatched histogram. Most show signs of moderate to heavy obscuration.

higher-energy X-rays (>10 keV), such as NuSTAR or Swift-BAT, are typically needed to detect low- or moderate-redshift AGNs under these extreme levels of obscuration (Koss et al. 2016; Lansbury et al. 2017).

4.5. Bolometric Luminosity Calculation

The total bolometric luminosity for each source is calculated by integrating the SED from the X-ray to the FIR. The gap in data between the X-ray and UV data is interpolated from the soft X-ray data point and the next-shortest-wavelength data point of the SED in log space. This region is unobservable owing to galactic and atmospheric absorption, and the models for the AGN and host galaxy emission are largely unconstrained. However, this linear interpolation provides a reasonable estimate of some contribution from this region without dominating the total bolometric luminosity of the source. For the sources with no FIR detections, the 1σ upper limit of the Herschel SPIRE data or the result from the stacking analysis is used in the calculation of the bolometric luminosity. The FIR can contribute more than 50% of the total bolometric luminosity for the less luminous sources in the sample; therefore, assuming the 1σ upper limit in the FIR may overestimate the bolometric luminosity for these sources with no FIR detections. However, these low-luminosity sources constitute <10% of our sample without FIR detections, and the bolometric luminosity of the more luminous sources, which tend to have the fewest FIR detections, is instead dominated by the UV to MIR emission. Therefore, any upper limits in the FIR will have a much smaller total effect on the bolometric luminosity (approximately 10% −25% of the total luminosity). The distribution of the total bolometric luminosity is shown in Figure 10.

In order to estimate the bolometric luminosity of the AGNs more accurately, a simple elliptical galaxy template from Assef et al. (2010) is subtracted from each source. While this template

spans 0.03–30 μm, it only reaches significant levels to contribute to the total luminosity between ∼0.3 and ∼3 μm. While AGNs are more likely to fall in systems with more star formation and stronger emission over a wider wavelength range than is represented in this template, removing a simple elliptical galaxy allows much of the stellar population from the host galaxy to be removed while ensuring that no UV, MIR, or FIR emission that may be originating from the nuclear region is inaccurately subtracted from the AGN luminosity. Though this may overestimate the AGN bolometric luminosity, particularly the contribution from the FIR, these calculations are not dependent on modeling the star formation histories of these systems.

The elliptical galaxy template is scaled to the 1 μm luminosity of each source, up to a maximum luminosity matching the average 1 μm luminosity in each redshift bin (see Figure 6). We do not allow the galaxy template to exceed this value, as the most luminous sources likely have contributions from the AGN emission at this wavelength (see Section 5.1 for further discussion of this emission component). For most sources, the elliptical galaxy component is a small fraction of the total bolometric luminosity; however, for some of the faint AGNs, this stellar component can be the main source of emission. While subtracting the elliptical galaxy component better estimates the total emission of the AGN, star formation within the host galaxy could still contribute significantly to the UV or FIR. Therefore, our integrated estimates can be considered as upper limits to the AGN bolometric luminosity for each system.

A central challenge in determining the AGN bolometric luminosity is to determine how much of the FIR emission is due to star formation and how much is from cold dust around the central nucleus. A more detailed fitting procedure that takes into account full AGN and star formation history models is necessary to properly disentangle the source(s) heating the dust. While such an analysis is beyond the scope of this paper, it is planned future work for a follow-up analysis of this sample. In the remainder of this work, we simply use the upper limit on the AGN bolometric luminosity.

We compare our bolometric luminosities to the X-ray-to-bolometric corrections for AGNs that have been reported in the literature. Figure 11 shows the ratio of the calculated AGN bolometric luminosity to the intrinsic X-ray luminosity as a function of the AGN bolometric luminosity. The sharp edge that is present at the upper left of the distribution is due to the lower limit of $L_{\rm X} > 10^{43}$ erg s^{-1} imposed on the sample. The literature relations from Duras et al. (2020) and Hopkins et al. (2007) are determined by fitting emission models to the SEDs of AGNs to calculate the AGN bolometric luminosity. Unlike our calculations, these models attribute much of the FIR emission to star formation rather than the AGN. Even with this difference, the literature relations generally agree with our calculated values in showing an increase in the ratio between the AGN bolometric luminosity and the intrinsic X-ray luminosity, with the least luminous sources showing a ratio of ∼10–20 and the most luminous sources showing a ratio of ∼80. While the average distribution in our sample is systematically larger than the bolometric corrections from the literature at high luminosities, there is large scatter in our distribution and the literature relations are consistent within the dispersion. Large scatter in the correction factor was analyzed in Vasudevan & Fabian (2007) and attributed to different classes of AGNs and AGN fitting techniques not taking the
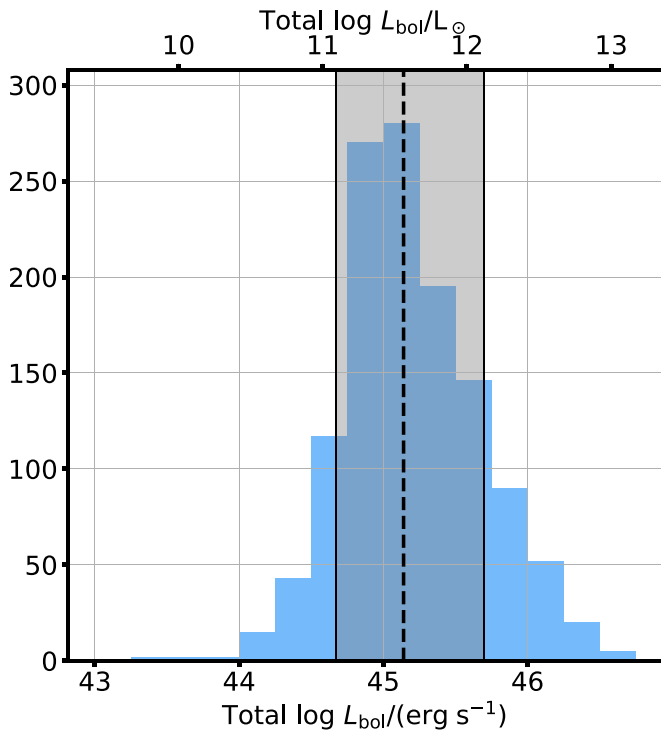
Figure 10. The distribution of the total bolometric luminosity found by integrating the X-ray to FIR SED of each AGN. The black dashed line shows the mean of log L_{bol}/(erg s^{-1}) = 45.2 distribution, and the shaded region shows the 1σ spread ±0.51 dex.

Figure 11. The X-ray bolometric correction, L_{bol}/L_X, as a function of the integrated bolometric luminosity. The black squares show the mean in bins of L_{bol}, with the error bars showing the 1σ spread in the y-direction and the width of the bin in the x-direction. The red and blue lines show bolometric corrections derived by Duras et al. (2020) and Hopkins et al. (2007), respectively. The average bolometric luminosity calculated in this work is systematically higher at high bolometric luminosities than the literature values.

fundamental properties of the AGNs into consideration, such as the SMBH mass. The offset between the literature values and the bolometric luminosity calculated in this work is also likely driven by the FIR luminosity. Duras et al. (2020) associate all emission beyond $\sim$50 μm with star formation; however, this cold dust component is included in our calculations.

We can instead fit the SED of the star-forming galaxy M82 (SFR $\sim$ 10 $M_{\odot}$ yr^{-1}) to each source, similarly scaling to the 1 μm luminosity in order to approximately match the stellar mass. With this fit, the bolometric correction matches more closely those derived by Hopkins et al. (2007) and Duras et al. (2020), lowering the median values plotted in Figure 11 by an average factor of $\sim$1.5. This effect is most significant for the less luminous sources in the sample, as the more luminous sources have bolometric luminosities driven by the AGN at all wavelengths. Removing the star-forming component by fitting the SED of M82 still leaves the average bolometric correction $\sim$0.15 dex higher on average than the literature values from Duras et al. (2020) for the most luminous AGNs.

We further test the contribution of the cold dust component by completely removing the FIR emission for all sources in our sample. This is done by truncating the integration of the SED at 15 μm, therefore removing all FIR emission and any dependency on upper limits or stacking in the L_{bol} calculation. When this cold dust component is completely removed from our AGN bolometric luminosity calculations, our average correction is closer to the Duras et al. (2020) and Hopkins et al. (2007) relations, though still a factor of $\sim$1.25 larger. The remaining offset likely comes from differences in the contributions to the AGN luminosity from the UV.

Without a more advanced fitting technique with an SED fitting routine such as CIGALE (Boquien et al. 2019; Yang et al. 2022), it is difficult to determine whether the AHA
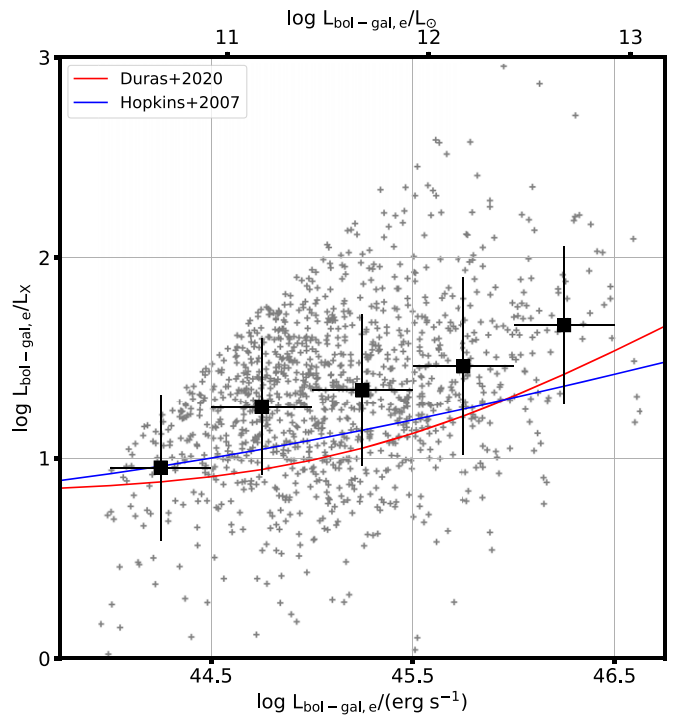
sources with the largest scatter above the literature relations truly have a large contribution in the FIR from the AGN, or whether the SED has a significant star-forming component. For now, the present calculations, with only the elliptical galaxy template removed, can be considered to be an upper limit on the AGN bolometric luminosity of the sample that will be used throughout the remainder of this analysis.

5. Discussion

While interesting correlations between X-rays and other AGN components can be seen in Figures 8 and 11, it can be challenging to disentangle these properties and correlate them with the three-dimensional circumnuclear environment around the SMBH. Here we discuss how the relations between UV and intrinsic X-ray luminosity and between MIR and X-ray luminosity provide insight into the evolution of an AGN and its circumnuclear dust as its accretion rate changes. A further analysis of observed SED properties is useful to interpret the different properties observed within the AHA AGN sample.

5.1. Characteristic SED Shapes

As discussed in Section 4.1, a wide range of SED shapes can be seen in all three redshift bins of Figure 5, with the UV and MIR emission spanning over two orders of magnitude in relative luminosity. While Figure 7 (SEDs sorted by luminosity) shows trends in SED shape with X-ray luminosity, there is still a wide range of SED emission features present at all luminosities. In order to better characterize the emission properties for such a diverse sample of AGNs and more clearly

Table 2
Criteria Used to Separate SEDs into Five Groups in Figure 12

Figure 12 (1)	(0.15–1.0 μm) (2)	(1.0–6.0 μm) (3)	(6.0–10 μm) (4)
First panel	$\alpha < -0.3$	$-0.4 < \alpha$	⋯
Second panel	$-0.3 < \alpha < 0.2$	$-0.4 < \alpha$	⋯
Third panel	$0.2 < \alpha$	$-0.4 < \alpha$	⋯
Fourth panel	$0.2 < \alpha$	$\alpha < -0.4$	$0.0 < \alpha$
Fifth panel	$0.2 < \alpha$	$\alpha < -0.4$	$\alpha < 0.0$

Note. Column (1): the panel in Figure 12. Column (2): UV slope. Columns (3)–(4): MIR slopes used to sort the SEDs. The spectral index, α, is defined via $F \propto \nu^{\alpha}$.

separate individual SED profiles, we now sort the AGNs based on the slope of their SEDs in the UV and the MIR, defined as α in Table 2. We create five distinct groups designed to capture the full range of SED properties present in the AHA sample and characterize AGNs by the relative strength of accretion disk emission and thermal reradiation from a dusty torus. Table 2 shows the definitions for each of the five groups, and Figure 12 shows the SEDs grouped accordingly. The panels are first defined by the slope of the observed UV continuum, where sources in the first panel have the strongest UV emission with a steep slope, sources in the second panel show moderate UV emission with a roughly flat slope, and sources in the bottom three panels show weak UV emission. This effectively acts as a proxy for the level of obscuration around the AGN (see further analysis in Section 5.4), as the UV emission is generated directly from the central accretion disk and is easily obscured by moderate amounts of dust. As the bottom three panels all show similar UV emission, they are further defined by their slope of the MIR continuum, which comes from warm dust heated by the AGN or young stars in the host galaxy.

Sources in the first panel of Figure 12 show an SED shape with the "classical" or "quasar-like" unobscured AGN features, such as a big blue bump in the UV and strong dusty torus emission. These AGNs also tend to have the highest intrinsic X-ray luminosity and fewest detections in the FIR. Sources in the second panel show a relatively flat SED shape with slightly lower X-ray luminosity and more FIR detections compared to the first panel. Sources in the bottom three panels consist primarily of obscured AGNs based on the lack of strong UV emission relative to the emission at 1 μm. Sources in the third panel show MIR emission that is increasing into the FIR, while sources in the fourth panel show MIR emission that is decreasing beyond 1 μm, before increasing again at $\sim$6 μm going into the FIR. Sources in the fifth panel show MIR emission that is continuing to decrease from $\sim$6 to 10 μm, before some increase again into the FIR, while others potentially continue to decrease or remain constant, as they have no FIR detection. The majority of AGNs have SED shapes matching those of obscured AGNs with high FIR emission (third and fourth panels), while the most luminous unobscured AGNs with quasar-like SEDs (first panel) constitute the smallest fraction of sources. This is consistent with the previous work that has shown that the majority of SMBH growth takes place in obscured AGNs (e.g., Treister et al. 2004, 2009; Hickox & Alexander 2018; Ananna et al. 2019) and reminds us that optically selected AGNs are far from representative of the full population.

While the FIR emission is not utilized when defining these SED panels, interesting insights can be gained based on the number of FIR detections in each panel. The number of FIR

detections peaks in the third and fourth panels and is substantially lower for the first, second, and fifth panels. While the first and second panels show similar emission features with moderate to strong emission in both the UV and MIR, the fifth panel shows vastly different properties with the weakest UV and MIR emission. This may imply that the cold dust component of these sources, which generates the FIR luminosity, may be low for two very different stages in the AGN life cycle, namely, when the luminosity is highest (the quasar phase) and when the luminosity had decreased and the AGN emission no longer dominated the emission of the host galaxy. Where these phases potentially fit in the life cycle of the AGN is discussed further in Section 5.5.

Figure 13 shows the distributions of the 1 μm luminosity used to normalize the SEDs in Figure 12. The distributions are roughly constant for the AGNs in the third through fifth panels. However, the sources from the second and first panels, which resemble increasingly less obscured and more powerful AGNs, have an average 1 μm luminosity that is 1.5 and 3 times higher than the average for the total distribution, respectively. This can also be seen in Figure 14, which shows the unnormalized median SED for each of the five panels.

The higher 1 μm luminosity for the first and second panel sources is likely caused by strong AGN emission, while for the bottom three panels the 1 μm luminosity is instead dominated by host galaxy emission. The median 1 μm luminosities for the SEDs in the bottom three panels match the average 1 μm luminosity for the entire sample shown in Figure 4, showing that the sources that fall in the first and second panels are the outliers on the upper end of this distribution. This steady increase in luminosity from the bottom three panels, to the second panel, to the first panel shows the increase of the AGN emission contribution to emission at all wavelengths.

Assuming that no significant AGN emission is contaminating the 1 μm luminosity for the bottom three panels, we can provide an estimate of the host galaxy stellar mass by following the scaling relation utilized in U et al (2012) for local galaxies. This leads to an approximate average stellar mass of $\log (M_*/M_\odot) \sim 10.8 \pm 0.35$ (FWHM). Such an estimation is much more challenging for the sources in the first and second panels with significant AGN contribution at 1 μm and requires a more detailed SED modeling procedure, which is beyond the scope of this work.

We also find that the redshift distribution for the bottom four panels (the median of which is displayed in Figures 13 and 15) is roughly constant, with only the first panel sources being found at preferentially higher redshifts. This may contribute to the increased luminosity of the first panel sources compared to the rest of the sample, seen in Figure 14.

Variations in the X-ray luminosity can be seen in Figure 15, which shows the distributions of the intrinsic X-ray luminosity for each panel. While the L_X distributions in the fourth and fifth panels are largely consistent with one another, the median X-ray luminosity begins to increase into the third panel and continues to increase through the second and first panels, with the first panel sources showing a median L_X nearly an order of magnitude larger than in the fourth and fifth panels. As an intrinsic X-ray luminosity this large must be generated directly from the central engine, this trend supports the conclusion that there is likely increased AGN activity in the unobscured sources in the first and second panels compared to those in the bottom three panels.
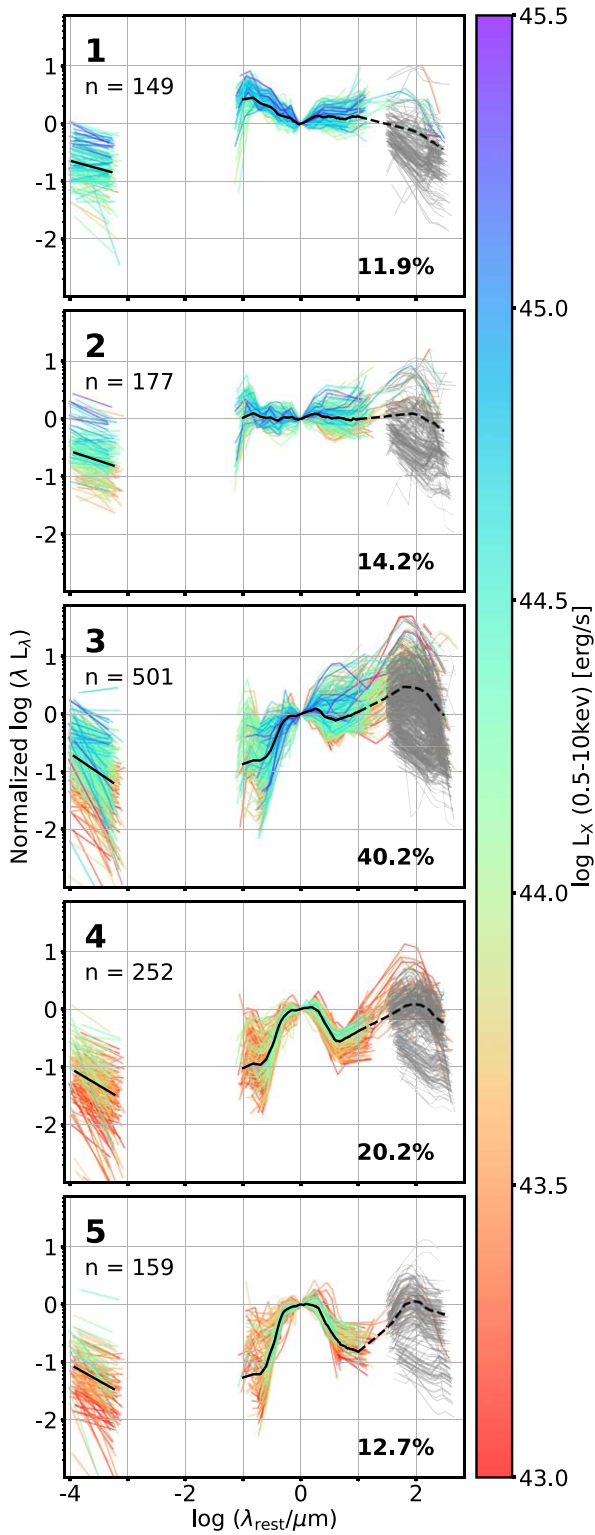
Figure 12. SEDs sorted into five panels based on UV and MIR emission properties (see Table 2). Each SED is normalized at rest-frame wavelength 1 μm and colored by the intrinsic 0.5–10 keV X-ray luminosity. The numbers indicate the number of AGNs in each panel and their percentage of the total sample. From top to bottom, the UV and MIR slopes change from falling to rising. Note: 8 sources out of 1246 (0.6%) are not included, as they fall outside the continuum slope limits, likely due to noise in the photometric data. Removing these sources has little no effect on the total analysis, as they are such a small fraction of the total sample.
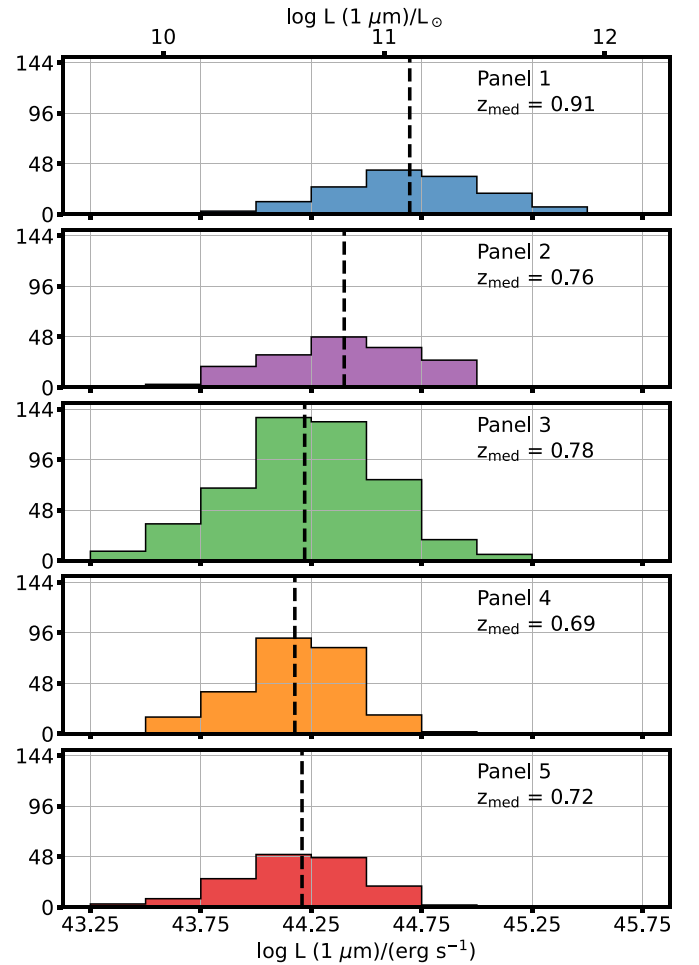
Figure 13. Distributions of 1 μm luminosities for the 1246 AGNs in our sample, separated according to the five SED shapes defined in Table 2 and shown in Figure 12. The median redshift of each panel is displayed in each panel, and the dashed black line shows the median 1 μm luminosity of each panel. The sources in the first panel have 1 μm luminosities 3 times higher than the other panels, indicating AGN dominance.

Hao et al. (2013) performed an analysis of unobscured AGNs in the COSMOS field to define a galaxy–AGN mixing sequence based on the slope of the SED at 0.3–1.0 μm and 1.0–3.0 μm. The mixing diagram was defined based on these slopes, with the unobscured quasars falling in the lower right corner of the diagram and sources with more reddening and a lower AGN fraction moving to the right of the diagram and up the diagram, respectively (see Bongiorno et al. 2012; Hao et al. 2013, for details and additional work). While we find general agreement with the interpretation of the five SEDs presented in this work and the previously defined mixing diagram, there are differences in the extent of the AGN contribution and the extent of the reddening by dust compared to our sample. We find that the second panel sources may have the AGN contribution at 1 μm overestimated in the mixing diagram, as well as the fourth panel sources showing more obscuration than may be predicted by Hao et al. (2013). However, there is general agreement between their proposed mixing sequence and the possible evolutionary sequence discussed later in this work.
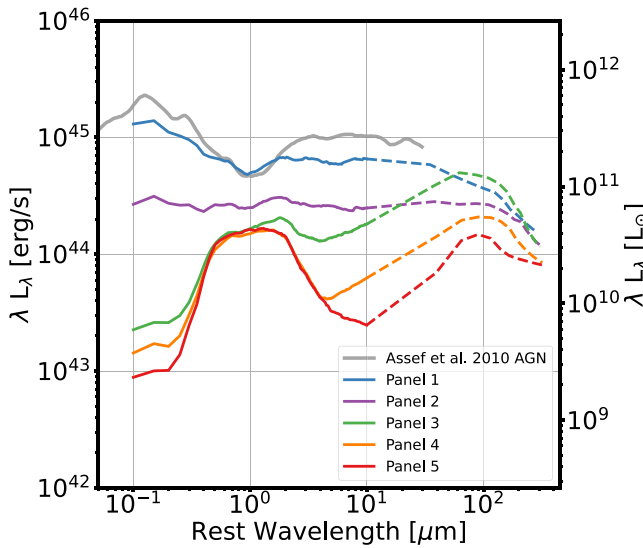
Figure 14. Median SEDs for the five panels shown in Figure 12. The FIR median lines include the 1σ upper limits for sources without FIR detections. The gray line shows an unobscured AGN template from Assef et al. (2010). Sources from the third through fifth panels have similar $1\,\mu$m luminosities, while the second and first panel sources have increasingly larger $1\,\mu$m luminosities, likely due to contributions from the AGN. Sources from the first panel are more luminous at all wavelengths from the X-ray to MIR than the sources from the other four panels.

Figure 15. Distributions of intrinsic X-ray luminosity for AGNs in each panel from Figure 12. The dashed black line shows the median X-ray luminosity of each panel. A clear trend can be seen, with the mean X-ray luminosity decreasing from the first panel to the fourth and fifth panels.

Figure 16. Ratio of UV (0.25 μm) luminosity to MIR (6 μm) luminosity as a function of MIR (6 μm) luminosity. Sources are colored based on which of the five panels in Figure 12 they fall into. The median of each of the five panels is shown as a large circle with the corresponding color for each panel, with the error bars showing the 75th and 25th percentiles of the distribution for each panel. Sources in the third panel have significantly weaker UV emission for a given MIR emission compared to the rest of the sample, likely driven by obscuration around the SMBH.
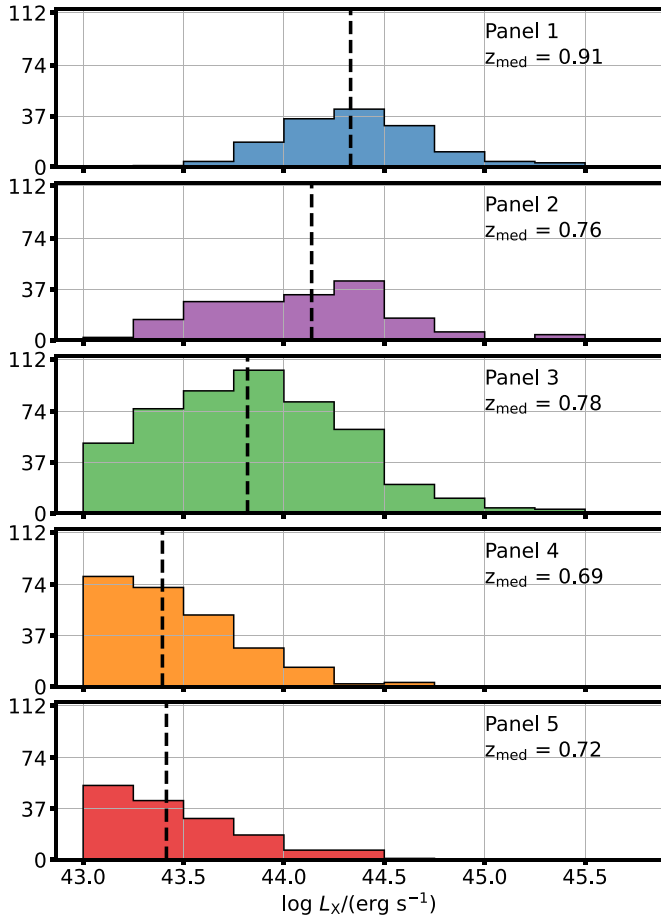
5.2. Accretion Disk and Dusty Torus Emission

We are interested in understanding how UV emission from the accretion disk and MIR emission from the dusty torus contribute to the observed AGN SED and how their relative contributions evolve with the growth of the SBMH. We use the five characteristic SED shapes to place these two emission components in context. Figure 16 shows the ratio between UV luminosity at $0.25\,\mu$m and MIR luminosity at $6\,\mu$m as a function of the $6\,\mu$m luminosity, while highlighting which of the five SED shapes each source belongs to. While a general trend of the UV-to-MIR ratio increasing with increasing MIR luminosity is present between the sources in the first, second, fourth, and fifth panels, the average location of the sources with SED shapes matching the third panel in Figure 12 have noticeably lower UV luminosities for a given MIR luminosity. The AGNs from the first and second panels, the most luminous and unobscured AGNs, tend to show the tightest correlation between the MIR and UV luminosity, while sources from the bottom three panels also show significantly more scatter. If we are to adopt an evolutionary sequence from the fourth panel to the first panel tracking the increasing intrinsic X-ray luminosity, we can infer that the MIR emission grows more rapidly than the observed UV emission, which is likely hidden behind significant levels of obscuration, leading to the increase in the MIR emission between the fourth and third panels. Once the obscuring dust is removed, potentially blown away by the AGN itself, the observed UV luminosity can increase rapidly, producing the relation seen between the sources in the first and second panels.

The top panel of Figure 17 shows the ratio between UV luminosity at $0.25\,\mu$m and the intrinsic X-ray luminosity as a function of the intrinsic X-ray luminosity, and the middle panel
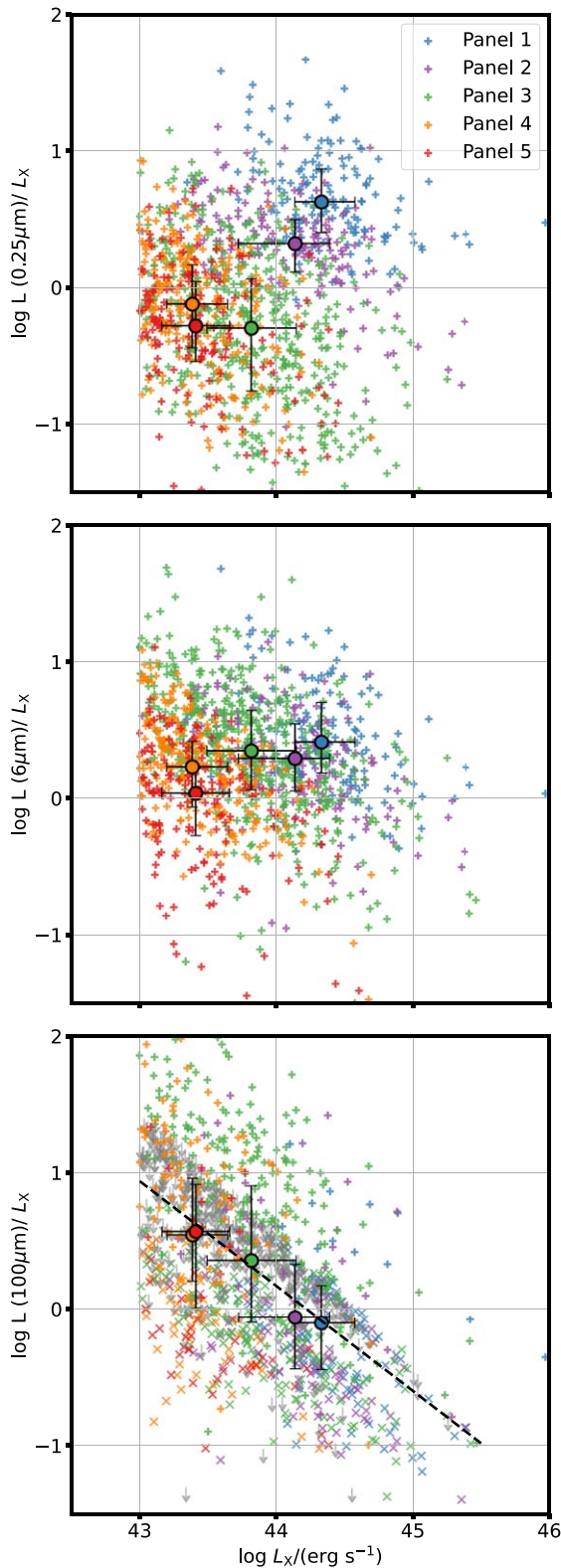
Figure 17. Ratio of UV (top), MIR (middle), and FIR (bottom) luminosity to intrinsic 0.5–10 keV X-ray luminosity as a function of intrinsic 0.5–10 keV X-ray luminosity. Colors correspond to the five panels in Figure 12. The median of each of the five panels is shown as a large circle, and error bars show the 75th and 25th percentiles of each distribution. The dashed line in the bottom panel is a fit to the data. The upper limits in the FIR are shown by downward-pointing arrows, and the crosses show the sources from Stripe 82X that utilize image stacking.

shows the same, but for the relation between the MIR and intrinsic X-ray luminosity. A similar trend to that seen in Figure 16 is seen between the UV and X-ray luminosity, with the sources in the first and second panels showing the largest UV luminosity for a given X-ray luminosity and the AGN from the third panel showing the largest offset from this relation. The large scatter for the more obscured sources in the bottom three panels is expected, as the UV luminosity will be much more heavily affected by moderate amounts of dust obscuration than the intrinsic X-ray luminosity, which has been corrected for this extinction. While the sources in panel 3 show intrinsic X-ray luminosities similar to those in the second panel, the much weaker UV emission is likely driven by this nuclear obscuration, as was the case in Figure 16. The effect of this nuclear obscuration is further investigated in Section 5.4.

A much more constant relation can be found between the MIR and X-ray emission in Figure 17, as was also seen in the middle panel of Figure 8. While large scatter is apparent, the average location of the sources in each SED shape bin is roughly constant. This is to be expected, as the MIR dust luminosity of an AGN has been shown to be tightly correlated with the intrinsic X-ray luminosity (e.g., Lutz et al. 2004; Fiore et al. 2009; Gandhi et al. 2009; Lanzuisi et al. 2009; Lusso et al. 2011; Asmus et al. 2015; Stern 2015). Figure 17 demonstrates that this is true of all AGNs within the largely unbiased AHA survey, regardless of the shape of the SED or the slope of the MIR emission. The distribution of all AGNs in the middle panel of Figure 17 shows significantly less scatter than is present in the UV-to-X-ray relation, and the shape of the SEDs follows a constant relation within the errors of the median. The strength of the MIR correlation with the intrinsic X-ray emission, regardless of the obscuration, shows that much of the IR emission cannot be singularly attributed to star formation; rather, much of it is likely powered by the AGN for the most X-ray-luminous source ($\log L_{\mathrm{X}}/(\mathrm{erg\,s}^{-1}) > 43$). This strong correlation between MIR and intrinsic X-ray luminosity emphasizes the need to determine how much MIR emission is powered by AGN heating and how much by young stars. Failing to account for MIR emission directly associated with the AGN will lead to overestimation of SFR (Kirkpatrick et al. 2017; Cooke et al. 2020).

5.3. Cold Dust Emission

The FIR emission from cold dust, whether powered by star formation within the host galaxy, by dust heated by the central engine, or by both, can now be analyzed in the context of the total SED shape defined in Section 5.1. In the bottom panel of Figure 17, the FIR/X-ray ratios decrease from the fourth and fifth panels at low X-ray luminosity to the lower first panel ratios at high X-ray luminosity. This strong downward trend is present both in the full sample and when just considering the sources with FIR detections. Figure 17 implies that the FIR luminosity must be roughly constant to moderately increasing for increasing X-ray luminosities, as was seen in Figure 8 and as the SED shapes show (Figure 12). Yang et al. (2019) showed a strong correlation for bulge-dominated galaxies between the black hole accretion rate and the SFR of X-ray-luminous AGNs, which traces a connection between the intrinsic X-ray luminosity and FIR luminosity. The much weaker correlation found in our data implies that the AHA

sample is not dominated by bulge or spheroidal galaxies and likely has many more disk galaxies, merging systems, or point sources. A detailed analysis of the host galaxies' morphology for each one of these sources is ongoing in the AHA collaboration (Schawinski et al. 2014; Powell et al. 2017; Ghosh et al. 2022; Tian et al. 2023).

Interpreting the exact connection between the AGN activity, which is traced by the intrinsic X-ray luminosity, and the cold dust emission in the FIR is challenging owing to the many additional factors that affect this relation. Changes in the dust mass of these systems and the covering factor of dust around the central engine will directly impact how much of the AGN emission can be reprocessed into the FIR. However, some interesting interpretation can still be made when examining the FIR emission in the context of the total SED shape. The low FIR luminosity and lack of FIR detections for many of the first and second panel AGNs with high X-ray and UV luminosities could be due to the powerful AGNs in these sources blowing away cold circumnuclear dust, changing the covering factor, and causing these sources to be less obscured and leading to weaker FIR emission than in the more heavily obscured sources found in the bottom three panels. This is consistent with the findings of Treister et al. (2008), Kirkpatrick et al. (2015), and Ananna et al. (2022a, 2022b) and would also imply that a significant component of the FIR luminosity seen in the sources in the bottom three panels is directly associated with the AGN, rather than with star formation in the host galaxy. While the lower relative FIR luminosity seen in the first and second panels could instead be associated with a decrease in the star formation of the host galaxy, perhaps driven by AGN feedback, Coleman et al. (2022) found no direct correlation between the X-ray luminosity and the dust mass of the host galaxy for AGNs in Stripe 82X at $z > 0.5$.

Ultimately, detailed SED modeling is necessary in order to determine the relative contributions in the FIR from AGNs and star formation in the host galaxy. Disentangling these two components is vital to understand the connection between AGN and host galaxy evolution. More sensitive FIR data, along with MIR spectroscopy, are ultimately necessary to remove the ambiguity caused by the upper limits and to properly determine the potential connection between the FIR emission and the central engine. Finally, spatially resolving where in the host galaxy the FIR emission is originating from could unambiguously determine whether the cold dust is directly associated with AGN activity.

5.4. Nuclear Obscuration

The total distribution of the obscuring column density, $N_{\rm H}$, for all sources that have the high-quality X-ray spectra necessary to determine $N_{\rm H}$ was shown in Section 4.4. We now bin these $N_{\rm H}$ measurements according to the shape of the SED defined in Section 5.1.

Figure 18 clearly shows the connection between estimated column density and SED shape: AGNs from the first and second panels have $N_{\rm H}$ values most consistent with unobscured AGNs (the peak of the distribution is $N_{\rm H} < 10^{22}$ cm^{-2}), while AGNs from the bottom three panels show much higher levels of obscuration, out to the Compton-thick regime ($N_{\rm H} > 10^{24}$ cm^{-2}). Figure 18 also shows that sources with low UV emission and large MIR emission (third panel sources) have the highest fraction of obscured AGNs. However, the individual sources with the highest $N_{\rm H}$ are in AGNs showing
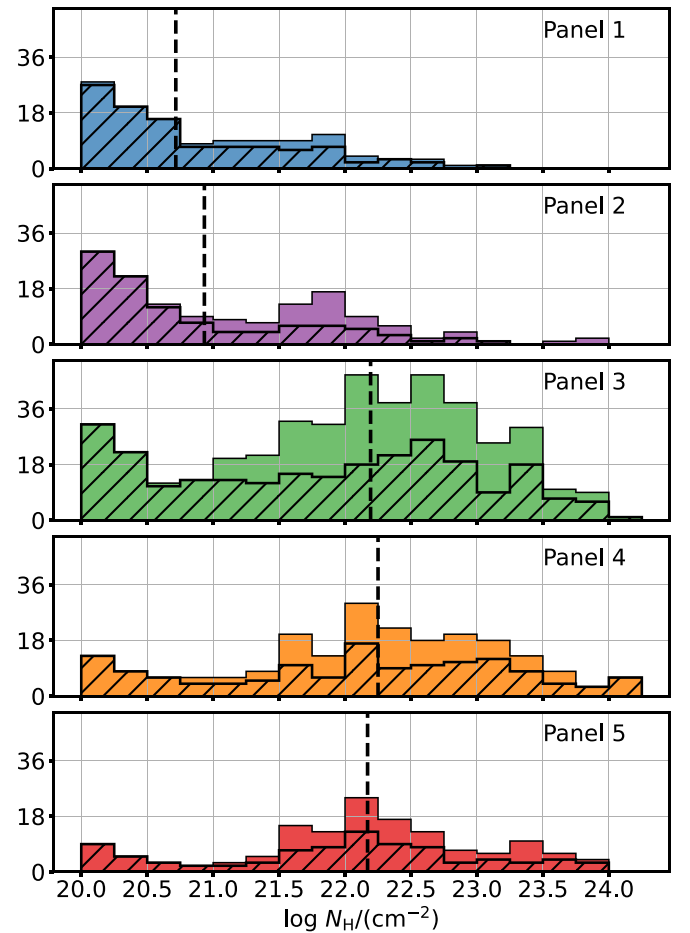

Figure 18. The distributions of the estimated column density, $N_{\rm H}$, for sources in each panel from Figure 12. The dashed black line is the median column density in each distribution for each panel. The total sample is shown in each respective color, while the measured estimates, without upper limits, are shown as the hatched histograms. AGNs from the first and second panels are mostly unobscured, while sources in the bottom three panels show a wide range of $N_{\rm H}$ values, from unobscured to Compton-thick.

lower relative MIR emission (fourth panel). An analysis of nearby merging galaxies by Ricci et al. (2021) showed that the fraction of heavily obscured AGNs peaks when the two galactic nuclei are at a separation of ~1 kpc. Within the context of this work, this may imply that a higher relative fraction of mergers may be present within the sources in the third panel, which show high levels of obscuration, along with large intrinsic X-ray emission (seen in Figure 15).

The observed trends discussed here construct an interesting picture of the emission properties of X-ray-luminous AGNs. The increasing intrinsic X-ray luminosity from the fourth and fifth panels to the first panel (Figure 15) and the relative levels of obscuration that peak in the third panel and sharply decrease in the first and second panels provide additional evidence of a direct connection to the intrinsic power of the AGN (traced by the intrinsic $L_{\rm X}$) and the covering factor of the obscuring dust around the central engine. As the AGN power increases, we find that the level of obscuration decreases. This is once again in agreement with previous work that provides an evolutionary connection between heavily obscured AGNs and unobscured quasars (e.g., Sanders et al. 1989; Lawrence 1991; DiMatteo et al. 2005; Hopkins et al. 2006; Oh et al. 2015; Ricci et al. 2017; Ananna et al. 2022a, 2022b).
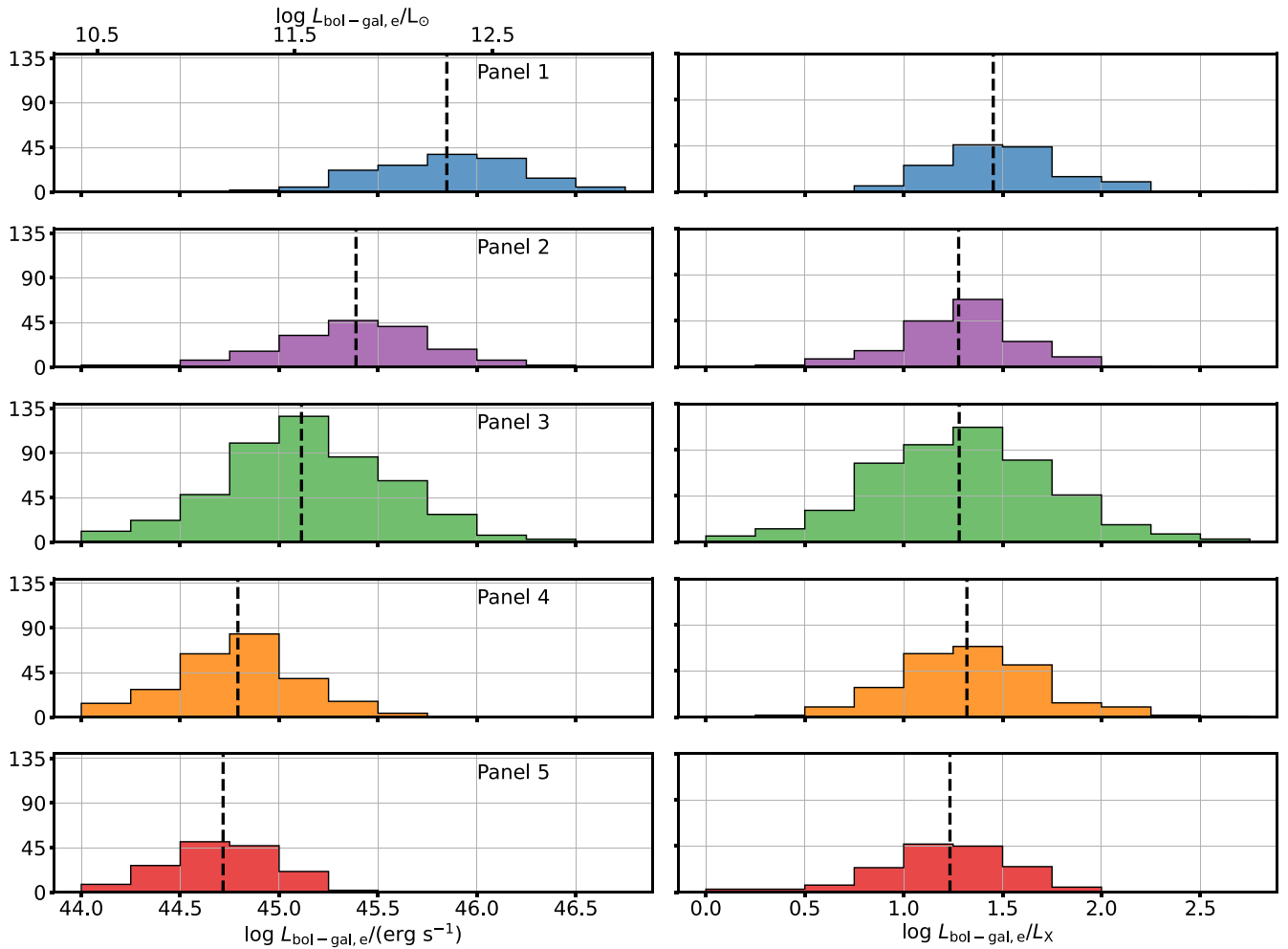
Figure 19. Left: distributions of the calculated bolometric luminosity (integrated X-ray to FIR minus the galaxy contribution) for AGNs in each panel from Figure 12. The dashed black line shows the median of each panel. A clear trend can be seen as the median bolometric luminosity decreasing from the first panel (blue) to the fifth panel (red). Right: ratio between the calculated AGN bolometric luminosity and intrinsic X-ray luminosity as a function of the SED shape defined in Table 2. The dashed black line shows the median ratios of each panel. This ratio is remarkably constant, independent of SED shape, indicating that X-ray luminosity is an excellent marker of total AGN power—and that accretion power dominates the energetics of these sources.

5.5. Bolometric Luminosity with SED Shape

The bolometric luminosity can now be analyzed in the context of SED shape. The left column of Figure 19 shows the distribution of bolometric luminosities for AGNs in each of the five panels. The median value increases by more than an order of magnitude between the fifth and first panels, with the greatest increase occurring between the second and first panels. As the first panel sources are the most luminous in the X-rays and show quasar-like SEDs, this simply indicates that X-ray power and bolometric power are correlated. It is also interesting to note that both the median and maximum bolometric luminosities are nearly equivalent for the unobscured sources in the second panel and the most heavily obscured sources in the third panel. This implies that we have recovered well the intrinsic X-ray luminosity, which in turn is correlated with the bolometric luminosity.

The right column of Figure 19 shows the distribution of bolometric corrections from the intrinsic X-ray luminosity (L_{bol}/L_X) for AGNs in each SED shape bin. The values are nearly constant across the five SED shapes. This means that the growth in bolometric luminosity seen in the left column of

Figure 19 is being driven by the AGN and is directly tied to the growth in the intrinsic X-ray luminosity shown in Figure 15. Despite this correspondence, the bolometric corrections are not small—most are in the range 8–100. This tight relation is perhaps surprising, given the wide range of SED shapes across the five panels. We can analyze which region of the SED is contributing most to the AGN bolometric luminosity for the AGNs in each of the five panels to better understand the evolution of the SEDs.

Figure 20 shows the ratios between the total bolometric luminosity of the sources and their UV, MIR, and FIR luminosities, as a function of total bolometric luminosity. It is clear that the bolometric luminosity is mostly dominated by the UV emission from the central accretion disk for the sources from the first and second panels. While the third panel sources have a median bolometric luminosity approaching that of the second panel AGNs, their direct UV contributions to L_{bol} are very low. This emission is instead reprocessed to MIR and FIR wavelengths, which dominate the contribution to L_{bol} for the third panel sources, as well as those in the fourth panel and some sources in the fifth panel.
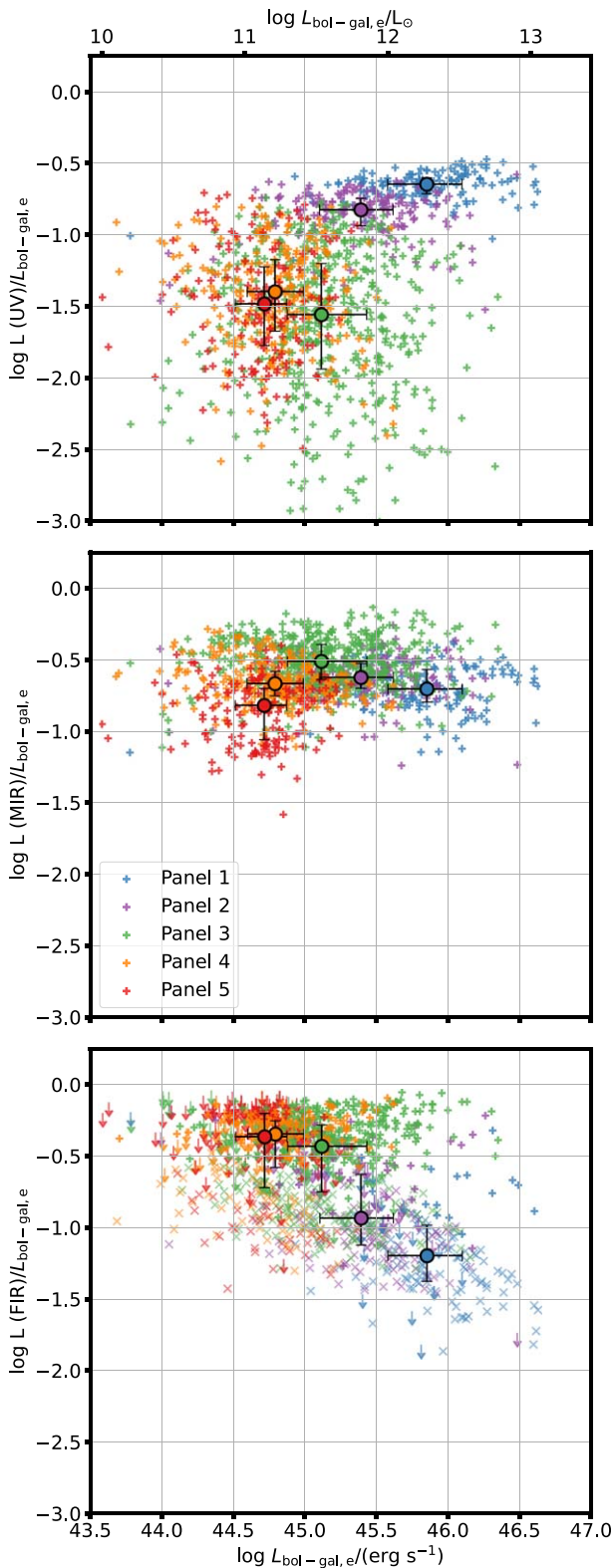
Figure 20. Top: ratio of UV (0.1–0.36 μm) to total bolometric luminosity as a function of bolometric luminosity, for the AHA AGN sample. Sources are colored according to their panel in Figure 12; medians are shown as large circles, and error bars indicate the 75th and 25th percentiles of the distributions. Middle: same as the top panel, but for MIR luminosity (3–30 μm). Bottom: same as the other two panels, but for FIR luminosity (30–500 μm). The upper limits in the FIR are shown by downward-pointing arrows, and the crosses show the sources from Stripe 82X that utilize image stacking.

Figure 20, along with the previous several figures, illustrates the similarity in the emission properties of the sources from the fourth and fifth panels. While these two SED shapes are distinguished by the 10 μm emission, the intrinsic properties (i.e., L_X, N_H, and L_{bol}), along with their UV (0.25 μm) and MIR (6 μm) emission, are remarkably similar. Therefore, at these luminosities, the 10 μm emission is unable to clearly distinguish AGN properties, unlike the other emission features analyzed throughout this work. This is likely due to the silicate absorption features and stronger host galaxy emission at this wavelength.

The transition from UV- to IR-dominated emission at a constant bolometric luminosity—i.e., from the third panel to the second panel—can be interpreted as further evidence of a possible evolutionary sequence between these five panels. As dusty obscured sources become more luminous with further AGN activity (transition from the fourth panel to the third panel), the luminous accretion disk may begin to sublimate and blow out some of the obscuring dust, decreasing the overall IR luminosity while increasing the observed UV luminosity (transition from the third panel to the second panel). Evidence of this removal of dust or receding dusty torus from the most actively accreting SMBHs has been recently shown by Ananna et al. (2022a, 2022b) and is in agreement with previous work showing that the obscured fraction of AGNs decreases with increasing bolometric luminosity (Lusso et al. 2013). Subsequently, AGNs continue to increase in total bolometric luminosity, with the UV component increasing significantly and the cold dust component decreasing (transition from the second panel to the first panel). AGNs with $L_{bol} > 10^{12.5}\ L_\odot$, which can be seen to the right in the bottom panel of Figure 20, may imply further evidence of this obscured-to-unobscured transition phase. The presence of several sources from the first three panels, at this high bolometric luminosity and high L (FIR)/L_{bol} fraction, may indicate the start of this transition, just before the cold dust component is removed and the FIR fraction drops, to the locus of the majority of the first panel sources. The implication is that much of the FIR emission is directly connected to the central engine, rather than to star formation in the host galaxy.

As previously stated, it is necessary to analyze both the intrinsic AGN and host galaxy properties through the use of detailed SED models that properly account for the AGN emission in the MIR and FIR to further analyze this potential evolutionary sequence. Additionally, the morphology of the host galaxies can shed light on this evolutionary sequence by identifying how it changes over the five characteristic SED shapes. Such an analysis is planned for a future work.

6. Conclusions

The combined fields of the AHA wedding-cake survey—Stripe 82X, COSMOS, and GOODS-N/S—provide a comprehensive sample of X-ray-selected AGNs, which is far less biased against obscured sources than optical or UV surveys. We have utilized the updated COSMOS2020 catalog (Weaver et al. 2022) and the most recent Stripe 82X X-ray analysis (Peca et al. 2023) to conduct a detailed multiwavelength analysis of X-ray-luminous AGNs in these three fields out to a redshift of $z_{spec} = 1.2$. We included AGNs with intrinsic 0.5–10 keV X-ray luminosity above $\log L_X/(\mathrm{erg\ s^{-1}}) > 43$.

Targets were carefully selected to ensure that each source has a secure spectroscopic redshift, that each source has an MIR detection near rest frame 6 μm, and that they are located in a field with FIR observations from Herschel SPIRE. This sample selection provides 1246 X-ray-luminous AGNs for the analysis. When visually inspecting the SEDs for these sources in three redshift bins, we find no major evolution in the multiwavelength properties and therefore do not separate the sources by redshift through the remainder of the analysis.

The main results of this analysis are as follows:

1. The full SED sample shows a wide range of observed rest-frame continuum strengths (relative to the 1 μm continuum), at wavelengths traditionally thought to be powered by the AGN: 3.5 (−3.2, +0.3) dex in the X-ray (5 keV), 2.6 (−2.0, +0.6) dex in the UV (0.25 μm), and 2.1 (−1.3, +0.8) dex in the MIR (6 μm). A similar range of relative continuum strengths, 2.8 (−1.2, +1.6) dex, is observed in the FIR (100 μm) when considering the upper limits.

2. The distribution of rest-frame 1 μm luminosity for the full sample is relatively narrow, with a mean luminosity log $L_{1\,\mu m}/(\mathrm{erg\ s^{-1}}) = 44.2 \pm 0.46$. Assuming that the 1 μm luminosity is dominated by the host galaxy (for all but the most luminous AGNs), we conclude that the host galaxies are primarily massive galaxies with mean mass log $(M_*/M_\odot) \sim 10.8 \pm 0.35$ (FWHM).

3. There is a positive, linear correlation between MIR (6 μm) luminosity and intrinsic X-ray luminosity, similar to Stern (2015). This suggests that the MIR emission is largely powered by the AGN. In contrast, only the most luminous AGNs in the UV show a positive correlation between the X-ray and UV luminosity. This implies that less luminous AGNs are far more likely to contain dust that suppresses the UV emission.

4. The calculated bolometric luminosities (X-ray to FIR, with an elliptical galaxy component subtracted) imply bolometric correction factors (L_{bol}/L_X) increasing from 10 to 70 over the range log $L_{\mathrm{bol}}/(\mathrm{erg\ s^{-1}}) = 44.5$–$46.5$. The trend of this correction is in agreement with Hopkins et al. (2007) and Duras et al. (2020) but is systematically higher by a factor of ∼1.8.

To explore the wide range of SED properties found in this sample of X-ray-luminous AGNs, we bin the SEDs based on the relative strengths of the UV (accretion disk) and MIR (dusty torus) emission, which we then relate to the intrinsic source properties, L_X, N_H, and L_{bol}. We identify five SED classes, shown in Figure 12. SEDs in the first panel have both strong UV and MIR emission, while the fifth panel has both weak UV and MIR emission. Only 11.9% of the AGNs fall in the first panel, with SEDs characteristic of unobscured quasars; 14.2% show "flat" SED shapes (second panel); 40.2% show weak UV and strong MIR emission (third panel); 20.2% show both weak UV and MIR emission, which then shows an increase toward the FIR (fourth panel); and 12.7% show both weak UV emission and MIR emission, which then decreases toward the FIR (fifth panel).

The following conclusions refer to the relation between these SED shapes and the AGN characteristics:

1. The intrinsic X-ray luminosity increases by 1.8 dex from the fourth and fifth panels to the first panel, implying that the unobscured, UV-luminous AGNs are intrinsically the most powerful AGNs.

2. The ratio L_{UV}/L_X increases with intrinsic X-ray luminosity; however, AGNs from the third panel show a significant offset from this relation, with weak UV luminosity for a given X-ray luminosity. Our analysis suggests that this is due to increased obscuration in the third panel AGNs. In contrast, the ratio L_{MIR}/L_X is constant with increasing X-ray luminosity, which is consistent with the MIR emission being less affected by obscuration. The ratio L_{FIR}/L_X decreases with increasing X-ray luminosity, consistent with relatively low to moderate contribution of the L_X to the L_{FIR}, dependent on the luminosity of the source and plausibly driven by the exact covering factor of cold dust around the central engine.

3. AGNs with weak UV emission and strong MIR emission (third panel) and those with weak UV and weak MIR (fourth panel) show the greatest levels and highest fraction of obscuration (mean log $N_H = 22.2$ [cm^{-1}]), while sources with strong UV and strong MIR emission show average levels of obscuration, more than an order of magnitude lower (mean log $N_H = 20.7$ [cm^{-1}]).

4. AGN bolometric luminosity increases with decreasing panel number, as the obscuration decreases, from low UV and MIR emission (fifth panel) to strong UV and MIR emission (first panel). The ratio between the intrinsic X-ray luminosity and the AGN bolometric luminosity is nearly constant for all SED shapes, with an average value of 20.8 ± 1.6. This is systematically higher than the AGN bolometric correction found by Duras et al. (2020) for all SED shapes.

Evidence for an AGN evolutionary sequence can be seen in the dependence of X-ray luminosity, obscuring column density, and bolometric luminosity on SED shape, as shown by Figures 15, 18, and 19. An X-ray-luminous AGN may begin as a low-luminosity, obscured AGN (fourth or fifth panel) before increasing in activity and therefore in X-ray luminosity (third panel). As AGN activity increases further, circumnuclear obscuring dust is removed, allowing the central accretion disk to become unobscured (first and second panels). After the accretion rate and X-ray luminosity decrease, the AGN may return to the fifth panel state once again. This evolutionary sequence is supported by the relative strengths of different AGN components for each SED shape (Figure 20). However, this is one interpretation of these SED profiles. It is also likely that not every AGN would undergo this full evolutionary sequence, and they may instead live their entire lives as low-luminosity obscured sources (fourth or fifth panel).

In order to fully explore this potential evolutionary sequence, it is vital to better understand how the AGN and host galaxy each contribute to the SED for each of these characteristic SED shapes. This can be explored through SED modeling with programs that properly account for the AGN emission at longer wavelengths, such as CIGALE (Boquien et al. 2019; Yang et al. 2020, 2022). It is also extremely important to include Compton-thick AGNs, which are mostly absent in this sample. Finally, analyzing the morphology of the host galaxy can provide unique insights into the evolutionary state of individual sources.

The AHA sample of AGNs has revealed a far broader range of SED shapes than is seen in optically or UV-selected samples

because of their bias against obscured sources. Traditional unobscured quasars constitute only about 10% of the AHA sample—and that is an overestimate given that we are still lacking the most heavily obscured, Compton-thick AGNs. Future AGN models need to explain the wide range of multiwavelength SEDs described here.

Acknowledgments

Appendix A
Sample Data

We present the data used to generate our SEDs for each of the 1246 AGNs in our sample. The tables below list the AHA field each source is located within, the data taken directly from the respective catalogs for each source (i.e., positional coordinates, photometry, X-ray luminosity, redshift, etc.), and new data calculated in this analysis, such as the bolometric luminosity and the characteristic shape of the SED discussed in Section 5.1.

Specifically, Table A1 lists the physical properties of each source. This includes the AHA field, ID (both from the X-ray and photometry catalog when available), positional coordinates of the X-ray source, intrinsic 0.5–10 keV X-ray luminosity, column density (N_H), and spectroscopic redshift. The references this information is acquired from are also listed in the table notes and described in more detail in Section 2. Table A1 additionally reports the calculated bolometric luminosity with the elliptical galaxy template from Assef et al. (2010) subtracted, as described in Section 4.5, and the SED shape classification it falls into based on Table 2 and Figure 12.

Tables A2, A3, and A4 list the AHA field, ID, and flux measurements used to create the SEDs for each source analyzed in this analysis in the Stripe 82X, COSMOS, and

Table A1
Characteristic Information of Each Source Used in This Analysis

AHA Field	X-Ray ID	Photometry ID	R.A.	Decl.	L_X (erg s^{-1})	z	N_H (cm^{-2})	L_{bol} (erg s^{-1})	Panel	Ref.
(1)	(2)	(3)	(4)	(5)	(6)	(7)	(8)	(9)	(10)	(11)
Stripe 82X	2407	2407	00h57m17.93907166 s	+00d32m44.37456608 s	44.11	0.492	22.48	45.58	1	[1], [2]
COSMOS	lid 1217	123228	09h59m45.0307 s	+01d28m28.6445 s	44.27	1.029	22.05	45.48	2	[3], [4]
GOODS-N	164	49309	12h36m21.22 s	+62d11m08.8 s	43.50	1.014	23.74	45.41	4	[5], [6], [9]
GOODS-S	806	2000	03h32m44.05056 s	−27d54m54.4176 s	43.88	0.908	22.60	43.62	3	[7], [8], [9]

Note. Column (1): the AHA field of the source. Column (2): the ID from the X-ray catalog. Column (3): the ID from the photometry catalog. Column (4): right ascension of the X-ray source. Column (5): decl. of the X-ray source. Column (6): log of the intrinsic X-ray luminosity. Column (7): the spectroscopic redshift. Column (8): log of the reported neutral hydrogen column density. Column (9): log of the galaxy-subtracted bolometric luminosity. Column (10): the panel from Figure 12 the source is sorted into. Column (11): references.
References. (1) Ananna et al. 2017; (2) Peca et al. 2023; (3) Weaver et al. 2022; (4) Marchesi et al. 2016a, 2016b; (5) Xue et al. 2016; (6) Barro et al. 2019; (7) Guo et al. 2013; (8) Luo et al. 2017; (9) Li et al. 2020. This table is available in its entirety in machine-readable form.

(This table is available in its entirety in machine-readable form.)

Table A2
The Photometric Data Used to Generate the Stripe 82X SEDs

AHA Field (1)	ID (2)	$F_{2-10keV}$ (3)	$F_{0.5-2keV}$ (4)	FUV (5)	FUV Err (6)	NUV (7)	NUV Err (8)	u (9)	...	SPIRE 500 (37)	SPIRE 500 Err (38)
Stripe 82X	2407	0.0039	0.00266	30.169	1.492	68.007	1.3834	95.406	...	−99.99	−99.99
Stripe 82X	2413	0.0038	0.0137	−99.99	−99.99	−99.99	−99.99	31.941	...	−99.99	−99.99
Stripe 82X	2420	0.00169	0.00346	−99.99	−99.99	−99.99	−99.99	2.7939	...	−99.99	−99.99
Stripe 82X	2435	0.00033	0.00064	−99.99	−99.99	−99.99	−99.99	35.191	...	27294.06	11242.11

Note. Column (1): the AHA field of the source. Column (2): the ID from the photometry catalog. Columns (3)–(38): The flux and flux errors from the listed band in μJy. Photometry comes from LaMassa et al. (2016), Ananna et al. (2017), and Peca et al. (2023) and is described in more detail in Section 2.1 and within each respective paper. Only a portion of the table is shown here. The entire table is available in its entirety in a machine-readable form.

(This table is available in its entirety in machine-readable form.)

Table A3
The Photometric Data Used to Generate the COSMOS SEDs

AHA Field (1)	ID (2)	$F_{2-10keV}$ (3)	$F_{0.5-2keV}$ (4)	FUV (5)	FUV Err (6)	NUV (7)	NUV Err (8)	u (9)	...	SPIRE 500 (45)	SPIRE 500 Err (46)
COSMOS	123228	9.92E-04	0.0041	−99.99	−99.99	5.71	0.1251	7.960	...	−99.99	−99.99
COSMOS	128954	0.00599	0.0158	1.438	0.078	4.72	0.0919	7.716	...	−99.99	−99.99
COSMOS	150058	0.0013	0.0021	1.521	0.079	13.85	0.1903	19.13	...	−99.99	−99.99
COSMOS	150214	0.0028	0.007	3.43	0.12	19.71	0.2183	17.87	...	7451.75	731.85

Note. Column (1): the AHA field of the source. Column (2): the ID from the photometry catalog. Columns (3)–(46): the flux and flux errors from the listed band in μJy. Photometry comes from Marchesi et al. (2016a, 2016b), Laigle et al. (2016); Lanzuisi et al. (2018), and Weaver et al. (2022) and is described in more detail in Section 2.2 and within each respective paper. Only a portion of the table is shown here. The entire table is available in its entirety in a machine-readable form.

(This table is available in its entirety in machine-readable form.)

Table A4
The Photometric Data Used to Generate the GOODS-N/S SEDs

AHA Field (1)	ID (2)	$F_{2-10keV}$ (3)	$F_{0.5-2keV}$ (4)	...	F435W (11)	F435W Err (12)	B (13)	B Err (14)	...	SPIRE 500 (67)	SPIRE 500 Err (68)
GOODS-N	48089	3.98E-04	0.00193	...	5.14	0.074	10.33	0.063	...	12435.0	2909.9
GOODS-N	49309	1.19E-04	2.4816E-05	...	0.284	0.037	0.345	0.046	...	6690.0	2230.0
GOODS-S	37812	4.653E-05	6.0661E-05	...	2.0975	0.06049	2.0976	0.0605	...	−99.99	−99.99
GOODS-S	30253	9.306E-05	1.4338E-04	...	0.5521	0.04247	0.5522	0.0425	...	18839	3070.8

Note. Column (1): the AHA field of the source. Column (2): the ID from the photometry catalog. Column (68): the flux from the listed band in μJy. The listed photometric IDs reference those from Yang et al. (2014) and Skelton et al. (2014) for GOODS-N and GOODS-S, respectively, with the photometric data derived from a combination of these catalogs with Liu et al. (2018), Barro et al. (2019), Elbaz et al. (2011), Oliver et al. (2012), Guo et al. (2013), and Hsu et al. (2014). These catalogs are described in more detail in Section 2.3 and within each respective paper. Only a portion of the table is shown here. The entire table is available in its entirety in a machine-readable form.

(This table is available in its entirety in machine-readable form.)

GOODS-N/S fields, respectively. Each field has been separated into different tables, as each field has a different set of observational filters making up the SEDs. The sources listed in these tables are the subsets of the total photometry catalogs used in this analysis. The original, complete catalogs for each field are described in Section 2, with the references additionally listed in the table notes. If there is a negative value in a photometric filter, either there were no data reported in the original catalog, or a data point with a high fractional error was reported and subsequently removed from the sample. When possible, these negative values are replaced in the analysis by either the upper limits reported in the original catalogs or the flux values resulting from the FIR image stacking analysis in Stripe 82X. It should also be noted that several of the original X-ray catalogs do not report formal errors on the X-ray fluxes. Reasonable values for such measurements were assumed for the analysis but are not reported in these tables. See the appropriate references listed in the tables and in Section 2 for more details on these X-ray fluxes and their uncertainties.

Appendix B
FIR Stacking for Stripe 82X

We employ an image stacking in order to achieve more accurate estimates of the FIR emission for the sources undetected in the Herschel images. For Stripe 82X AGNs, sources were grouped in bins of redshift and the observed WISE W4 (22 μm) luminosity. There are 22 sources with no W4 detections. These sources were placed into a separate bin (bin 8 in Table B1) so that the majority of the sources could still be grouped by their MIR luminosity. The Herschel SPIRE 250 μm images were then stacked for each bin at the locations of the optical coordinates for each source. The flux measurements were then made through bootstrapping 10,000
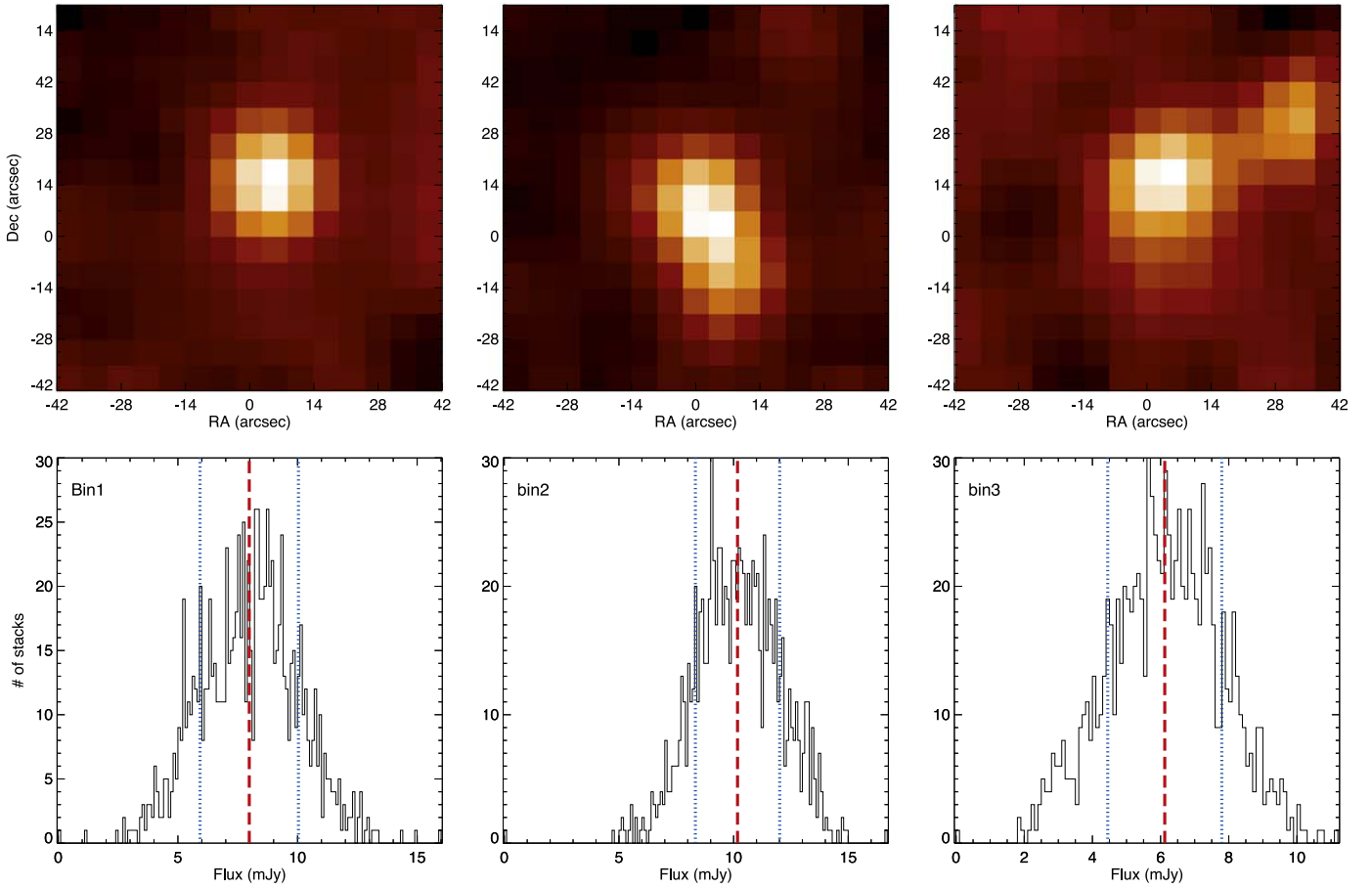
Figure 21. Top: stacked images of the first three bins from the 250 μm images. Bottom: histograms of the flux measurements made from 10,000 bootstrapped stacks for the corresponding images in the top row.

Table B1
The Results from the Stripe 82X 250 μm Stacking Procedure

Bin Number	z Limits	log L (22 μm) Limits (erg s^{-1})	N	Average z	$S_{250\mu m}$ (mJy)	$dS_{250\mu m}$ (mJy)
(1)	(2)	(3)	(4)	(5)	(6)	(7)
Bin 1	0.00–0.40	0.00—44.0	66	0.28	7.98	2.06
Bin 2	0.00–0.40	44.0—47.0	68	0.35	10.17	1.84
Bin 3	0.40–0.70	0.00—44.5	95	0.50	6.12	1.67
Bin 4	0.40–0.70	44.5—47.0	53	0.61	9.14	2.35
Bin 5	0.70—1.05	0.00—45.0	107	0.85	4.26	1.44
Bin 6	0.70—1.05	45.0—47.0	39	0.93	14.93	3.76
Bin 7	1.05–1.25	0.00—47.0	49	1.13	9.92	2.75
Bin 8	0.00—1.25	0.00–0.00	22	0.91	15.74	5.40

Notes. Column (1): the bin number. Column (2): the redshift range for each bin. Column (3): the luminosity from the W4 band. Column (4): number of sources in each bin. Column (5): average redshift of each bin. Column (6): the resulting 250 μm flux from each bin. Column (7): the error in the resulting 250 μm found from bootstrapping.

runs per bin. This stacking procedure was then repeated on random positions in order determine the error in the stacked detection threshold. This is a similar process to what was done in Stanley et al. (2017) and Coleman et al. (2022).

Table B1 shows information for each bin and the results from the stacking analysis. Figure 21 shows three examples of the final stacked images and histograms of the flux measurements resulting from 10,000 bootstrapped stacks.

This same process was attempted for the sources in the COSMOS field that lack detections at 250 μm; however,

because of the depth of the Herschel images in this field, no signal can be determined that is above the 2σ limit of the background noise. A similar problem is found for the sources in GOODS-N/S owing to the depth of the Herschel images and the small number of sources lacking detections at 250 μm that can be used for stacking in each bin. Therefore, no stacking procedure is employed for the sources in COSMOS and GOODS-N/S in the analysis, and the upper limits reported in each respective catalog are used instead, as described in Section 3.2.

THE ASTROPHYSICAL JOURNAL, 957:19 (24pp), 2023 November 1

Auge et al.

ORCID iDs

Connor Auge https://orcid.org/0000-0002-5504-8752
David Sanders https://orcid.org/0000-0002-1233-9998
Ezequiel Treister https://orcid.org/0000-0001-7568-6412
C. Megan Urry https://orcid.org/0000-0002-0745-9792
Allison Kirkpatrick https://orcid.org/0000-0002-1306-1545
Nico Cappelluti https://orcid.org/0000-0002-1697-186X
Tonima Tasnim Ananna https://orcid.org/0000-0001-8211-3807
Médéric Boquien https://orcid.org/0000-0003-0946-6176
Mislav Baloković https://orcid.org/0000-0003-0476-6647
Francesca Civano https://orcid.org/0000-0002-2115-1137
Brandon Coleman https://orcid.org/0000-0003-3930-7950
Aritra Ghosh https://orcid.org/0000-0002-2525-9647
Jeyhan Kartaltepe https://orcid.org/0000-0001-9187-3605
Michael Koss https://orcid.org/0000-0002-7998-9581
Stephanie LaMassa https://orcid.org/0000-0002-5907-3330
Stefano Marchesi https://orcid.org/0000-0001-5544-0749
Alessandro, Peca https://orcid.org/0000-0003-2196-3298
Meredith Powell https://orcid.org/0000-0003-2284-8603
Benny Trakhtenbrot https://orcid.org/0000-0002-3683-7297
Tracey Jane Turner https://orcid.org/0000-0003-2971-1722

References

Alexander, D. M., Bauer, F. E., Brandt, W. N., et al. 2003, AJ, 126, 539
Ananna, T. T., Salvato, M., LaMassa, S., et al. 2017, ApJ, 850, 66
Ananna, T. T., Treister, E., Urry, C. M., et al. 2019, ApJ, 871, 240
Ananna, T. T., Urry, C. M., Ricci, C., et al. 2022a, ApJL, 939, L13
Ananna, T. T., Weigel, A. K., Trakhtenbrot, B., et al. 2022b, ApJS, 261, 9
Asmus, D., Gandhi, P., Hönig, S. F., Smette, A., & Duschl, W. J. 2015, MNRAS, 454, 766
Asmus, D., Hönig, S. F., & Gandhi, P. 2016, ApJ, 822, 109
Assef, R. J., Eisenhardt, P. R. M., Stern, D., et al. 2015, ApJ, 804, 27
Assef, R. J., Kochanek, C. S., Brodwin, M., et al. 2010, ApJ, 713, 970
Assef, R. J., Stern, D., Kochanek, C. S., et al. 2013, ApJ, 772, 26
Astropy Collaboration, Price-Whelan, A. M., Sipőcz, B. M., et al. 2018, AJ, 156, 123
Astropy Collaboration, Robitaille, T. P., Tollerud, E. J., et al. 2013, A&A, 558, A33
Barger, A. J., Cowie, L. L., Owen, F. N., et al. 2015, ApJ, 801, 87
Barro, G., Pérez-González, P. G., Cava, A., et al. 2019, ApJS, 243, 22
Bassani, L., Dadina, M., Maiolino, R., et al. 1999, ApJS, 121, 473
Becker, R. H., White, R. L., & Helfand, D. J. 1995, ApJ, 450, 559
Bongiorno, A., Merloni, A., Brusa, M., et al. 2012, MNRAS, 427, 3103
Boquien, M., Burgarella, D., Roehlly, Y., et al. 2019, A&A, 622, A103
Brandt, W. N., & Alexander, D. M. 2015, A&ARv, 23, 1
Cappelluti, N., Brusa, M., Hasinger, G., et al. 2009, A&A, 497, 635
Cappelluti, N., Hasinger, G., Brusa, M., et al. 2007, ApJS, 172, 341
Carroll, C. M., Hickox, R. C., Masini, A., et al. 2021, ApJ, 908, 185
Carroll, C. M., Ananna, T. T., Hickox, R. C., et al. 2023, ApJ, 950, 127
Casali, M., Adamson, A., Alves de Oliveira, C., et al. 2007, A&A, 467, 777
Civano, F., Marchesi, S., Comastri, A., et al. 2016, ApJ, 819, 62
Coleman, B., Kirkpatrick, A., Cooke, K. C., et al. 2022, MNRAS, 515, 82
Cooke, K. C., Kirkpatrick, A., Estrada, M., et al. 2020, ApJ, 903, 106
Damen, M., Labbé, I., van Dokkum, P. G., et al. 2011, ApJ, 727, 1
DiMatteo, T., Springel, V., & Hernquist, L. 2005, Natur, 433, 604
Donley, J. L., Koekemoer, A. M., Brusa, M., et al. 2012, ApJ, 748, 142
Duras, F., Bongiorno, A., Ricci, F., et al. 2020, A&A, 636, A73
Elbaz, D., Dickinson, M., Hwang, H. S., et al. 2011, A&A, 533, A119
Elvis, M., Civano, F., Vignali, C., et al. 2009, ApJS, 184, 158
Elvis, M., Hao, H., Civano, F., et al. 2012, ApJ, 759, 6
Fabbiano, G., Gioia, I. M., & Trinchieri, G. 1989, ApJ, 347, 127
Fan, X., Strauss, M. A., Schneider, D. P., et al. 2003, AJ, 125, 1649
Fiore, F., Puccetti, S., Brusa, M., et al. 2009, ApJ, 693, 447
Fliri, J., & Trujillo, I. 2016, MNRAS, 456, 1359
Gandhi, P., Horst, H., Smette, A., et al. 2009, A&A, 502, 457
Ghosh, A., Urry, C. M., Rau, A., et al. 2022, ApJ, 935, 138

Giavalisco, M., Ferguson, H. C., Koekemoer, A. M., et al. 2004, ApJL, 600, L93
Gilli, R., Norman, C., Calura, F., et al. 2022, A&A, 666, A17
Goulding, A. D., Alexander, D. M., Bauer, F. E., et al. 2012, ApJ, 755, 5
Grogin, N. A., Kocevski, D. D., Faber, S. M., et al. 2011, ApJS, 197, 35
Guo, Y., Ferguson, H. C., Giavalisco, M., et al. 2013, ApJS, 207, 24
Hao, H., Elvis, M., Bongiorno, A., et al. 2013, MNRAS, 434, 3104
Hao, H., Elvis, M., Civano, F., et al. 2014, MNRAS, 438, 1288
Harris, C. R., Millman, K. J., van der Walt, S. J., et al. 2020, Natur, 585, 357
Hasinger, G., Capak, P., Salvato, M., et al. 2018, ApJ, 858, 77
Heckman, T. M., & Best, P. N. 2014, ARA&A, 52, 589
Heckman, T. M., Ptak, A., Hornschemeier, A., & Kauffmann, G. 2005, ApJ, 634, 161
Helfand, D. J., White, R. L., & Becker, R. H. 2015, ApJ, 801, 26
Hewett, P. C., Warren, S. J., Leggett, S. K., & Hodgkin, S. T. 2006, MNRAS, 367, 454
Hickox, R. C., & Alexander, D. M. 2018, ARA&A, 56, 625
Hickox, R. C., & Markevitch, M. 2007, ApJL, 661, L117
Hopkins, P. F., Cox, T. J., Kereš, D., & Hernquist, L. 2008, ApJS, 175, 390
Hopkins, P. F., Richards, G. T., & Hernquist, L. 2007, ApJ, 654, 731
Hopkins, P. F., Somerville, R. S., Hernquist, L., et al. 2006, ApJ, 652, 864
Hsu, L.-T., Salvato, M., Nandra, K., et al. 2014, ApJ, 796, 60
Hunter, J. D. 2007, CSE, 9, 90
Hviding, R. E., Hainline, K. N., Rieke, M., et al. 2022, AJ, 163, 224
Ichikawa, K., Packham, C., Ramos Almeida, C., et al. 2015, ApJ, 803, 57
Jiang, L., Fan, X., Bian, F., et al. 2014, ApJS, 213, 12
Jin, S., Daddi, E., Liu, D., et al. 2018, ApJ, 864, 56
Just, D. W., Brandt, W. N., Shemmer, O., et al. 2007, ApJ, 665, 1004
Kirkpatrick, A., Alberts, S., Pope, A., et al. 2017, ApJ, 849, 111
Kirkpatrick, A., Pope, A., Sajina, A., et al. 2015, ApJ, 814, 9
Koekemoer, A. M., Faber, S. M., Ferguson, H. C., et al. 2011, ApJS, 197, 36
Kormendy, J., & Ho, L. C. 2013, ARA&A, 51, 511
Koss, M. J., Assef, R., Baloković, M., et al. 2016, ApJ, 825, 85
Lacy, M., Ridgway, S. E., Gates, E. L., et al. 2013, ApJS, 208, 24
Lacy, M., Storrie-Lombardi, L. J., Sajina, A., et al. 2004, ApJS, 154, 166
Laigle, C., McCracken, H. J., Ilbert, O., et al. 2016, ApJS, 224, 24
LaMassa, S. M., Urry, C. M., Cappelluti, N., et al. 2013a, MNRAS, 436, 3581
LaMassa, S. M., Urry, C. M., Cappelluti, N., et al. 2016, ApJ, 817, 172
LaMassa, S. M., Urry, C. M., Glikman, E., et al. 2013b, MNRAS, 432, 1351
Lang, D., Hogg, D. W., & Schlegel, D. J. 2016, AJ, 151, 36
Lansbury, G. B., Alexander, D. M., Aird, J., et al. 2017, ApJ, 846, 20
Lanzuisi, G., Civano, F., Marchesi, S., et al. 2018, MNRAS, 480, 2578
Lanzuisi, G., Piconcelli, E., Fiore, F., et al. 2009, A&A, 498, 67
Lawrence, A. 1991, MNRAS, 252, 586
Lawrence, A., Warren, S. J., Almaini, O., et al. 2007, MNRAS, 379, 1599
Li, J., Xue, Y., Sun, M., et al. 2020, ApJ, 903, 49
Liu, D., Daddi, E., Dickinson, M., et al. 2018, ApJ, 853, 172
Luo, B., Brandt, W. N., Xue, Y. Q., et al. 2017, ApJS, 228, 2
Lusso, E., Comastri, A., Vignali, C., et al. 2011, A&A, 534, A110
Lusso, E., Hennawi, J. F., Comastri, A., et al. 2013, ApJ, 777, 86
Lusso, E., & Risaliti, G. 2017, A&A, 602, A79
Lutz, D., Mainieri, V., Rafferty, D., et al. 2010, ApJ, 712, 1287
Lutz, D., Maiolino, R., Spoon, H. W. W., & Moorwood, A. F. M. 2004, A&A, 418, 465
Marchesi, S., Civano, F., Elvis, M., et al. 2016a, ApJ, 817, 34
Marchesi, S., Lanzuisi, G., Civano, F., et al. 2016b, ApJ, 830, 100
Markowitz, A. G., Krumpe, M., & Nikutta, R. 2014, MNRAS, 439, 1403
McKinney, J., Hayward, C. C., Rosenthal, L. J., et al. 2021, ApJ, 921, 55
McMahon, R. G., Banerji, M., Gonzalez, E., et al. 2013, Msngr, 154, 35
Morrissey, P., Conrow, T., Barlow, T. A., et al. 2007, ApJS, 173, 682
Mullaney, J. R., Daddi, E., Béthermin, M., et al. 2012, ApJL, 753, L30
Nandra, K., & Pounds, K. A. 1994, MNRAS, 268, 405
Netzer, H. 2015, ARA&A, 53, 365
Neugebauer, G., Soifer, B. T., Matthews, K., & Elias, J. H. 1989, AJ, 97, 957
Oh, K., Yi, S. K., Schawinski, K., et al. 2015, ApJS, 219, 1
Oliver, S. J., Bock, J., Altieri, B., et al. 2012, MNRAS, 424, 1614
Page, M. J., Symeonidis, M., Vieira, J. D., et al. 2012, Natur, 485, 213
Papovich, C., Shipley, H. V., Mehrtens, N., et al. 2016, ApJS, 224, 28
Peca, A., Cappelluti, N., Urry, M., et al. 2023, ApJ, 943, 162
Perez, F., & Granger, B. E. 2007, CSE, 9, 21
Persic, M., Rephaeli, Y., Braito, V., et al. 2004, A&A, 419, 849
Powell, M. C., Urry, C. M., Cardamone, C. N., et al. 2017, ApJ, 835, 22
Ramos Almeida, C., Levenson, N. A., Alonso-Herrero, A., et al. 2011, ApJ, 731, 92
Ramos Almeida, C., Levenson, N. A., Rodríguez Espinosa, J. M., et al. 2009, ApJ, 702, 1127
Ranalli, P., Comastri, A., & Setti, G. 2003, A&A, 399, 39

Ricci, C., Privon, G. C., Pfeifle, R. W., et al. 2021, MNRAS, 506, 5935
Ricci, C., Trakhtenbrot, B., Koss, M. J., et al. 2017, Natur, 549, 488
Richards, G. T., Nichol, R. C., Gray, A. G., et al. 2004, ApJS, 155, 257
Rovilos, E., Comastri, A., Gilli, R., et al. 2012, A&A, 546, A58
Sanders, D. B., Phinney, E. S., Neugebauer, G., Soifer, B. T., & Matthews, K. 1989, ApJ, 347, 29
Sanders, D. B., Soifer, B. T., Elias, J. H., Neugebauer, G., & Matthews, K. 1988, ApJL, 328, L35
Santini, P., Rosario, D. J., Shao, L., et al. 2012, A&A, 540, A109
Schawinski, K., Urry, C. M., Simmons, B. D., et al. 2014, MNRAS, 440, 889
Schneider, D. P., Hall, P. B., Richards, G. T., et al. 2005, AJ, 130, 367
Scoville, N., Aussel, H., Brusa, M., et al. 2007, ApJS, 172, 1
Skelton, R. E., Whitaker, K. E., Momcheva, I. G., et al. 2014, ApJS, 214, 24
Stalevski, M., Asmus, D., & Tristram, K. R. W. 2017, MNRAS, 472, 3854
Stanley, F., Alexander, D. M., Harrison, C. M., et al. 2017, MNRAS, 472, 2221
Steffen, A. T., Strateva, I., Brandt, W. N., et al. 2006, AJ, 131, 2826
Stern, D. 2015, ApJ, 807, 129
Stern, D., Eisenhardt, P., Gorjian, V., et al. 2005, ApJ, 631, 163
Straatman, C. M. S., Spitler, L. R., Quadri, R. F., et al. 2016, ApJ, 830, 51
Suh, H., Civano, F., Hasinger, G., et al. 2019, ApJ, 872, 168

Sutherland, W., & Saunders, W. 1992, MNRAS, 259, 413
Symeonidis, M., Giblin, B. M., Page, M. J., et al. 2016, MNRAS, 459, 257
Tian, C., Urry, C. M., Ghosh, A., et al. 2023, ApJ, 944, 124
Timlin, J. D., Ross, N. P., Richards, G. T., et al. 2016, ApJS, 225, 1
Treister, E., Krolik, J. H., & Dullemond, C. 2008, ApJ, 679, 140
Treister, E., Urry, C. M., Chatzichristou, E., et al. 2004, ApJ, 616, 123
Treister, E., Urry, C. M., & Virani, S. 2009, ApJ, 696, 110
U, V., Sanders, D. B., Mazzarella, J. M., et al. 2012, ApJS, 203, 9
Vasudevan, R. V., & Fabian, A. C. 2007, MNRAS, 381, 1235
Viero, M. P., Asboth, V., Roseboom, I. G., et al. 2014, ApJS, 210, 22
Virtanen, P., Gommers, R., Oliphant, T. E., et al. 2020, NatMe, 17, 261
Weaver, J. R., Kauffmann, O. B., Ilbert, O., et al. 2022, ApJS, 258, 11
Wright, E. L., Eisenhardt, P. R. M., Mainzer, A. K., et al. 2010, AJ, 140, 1868
Xue, Y. Q. 2017, NewAR, 79, 59
Xue, Y. Q., Luo, B., Brandt, W. N., et al. 2016, ApJS, 224, 15
Yan, W., Hickox, R. C., Hainline, K. N., et al. 2019, ApJ, 870, 33
Yang, G., Boquien, M., Brandt, W. N., et al. 2022, ApJ, 927, 192
Yang, G., Boquien, M., Buat, V., et al. 2020, MNRAS, 491, 740
Yang, G., Brandt, W. N., Alexander, D. M., et al. 2019, MNRAS, 485, 3721
Yang, G., Chen, C. T. J., Vito, F., et al. 2017, ApJ, 842, 72
Yang, G., Xue, Y. Q., Luo, B., et al. 2014, ApJS, 215, 27